Optogenetic control of pheromone gradients and mating behavior in budding yeast

Alvaro Banderas[1,4,*], Maud Hofmann[1], Céline Cordier[1], Matthias Le Bec[1], M Carolina Elizondo-Cantú[1], Lionel Chiron[1], Sylvain Pouzet[1], Yotam Lifschytz[3], Wencheng Ji[3], Ariel Amir[3], Vittore Scolari[1,2,†,*] and Pascal Hersen[1,†,*]

[1] *Institut Curie, Université PSL, Sorbonne Université, CNRS UMR168, Physics of Cells and Cancer, 75005 Paris, France*

[2] *Institut Curie, Université PSL, Sorbonne Université, CNRS UMR3664, Laboratoire Dynamique du Noyau, 75005 Paris, France*

[3] *Department of Physics of Complex Systems, Weizmann Institute of Science, 234 Hertzl St., Rehovot, Israel*

[4] *INM - Leibniz Institute for New Materials, Campus D2 2, 66123 Saarbrücken, Germany.*

[†] *These authors contributed equally to this work*

**Corresponding authors: alvaro.banderas@leibniz-inm.de, vittore.scolari@curie.fr, pascal.hersen@curie.fr*

Keywords: Optogenetics, Mating, Budding Yeast, Cell-cell communication, Pheromone, Reaction-Diffusion, Gradients

Abstract

During mating in budding yeast, cells use pheromones to locate each other and fuse. This model system has shaped our current understanding of signal transduction and cell polarization in response to extracellular signals. The cell-population produced extracellular signal landscapes themselves are however less well understood, yet crucial for functionally testing quantitative

models of cell polarization and for controlling cell behavior through bioengineering approaches. Here we engineered optogenetic control of pheromone landscapes in mating populations of budding yeast, hijacking the mating-pheromone pathway to achieve spatial control of growth, cell morphology, cell-cell fusion, and distance-dependent gene expression in response to light. Using our tool, we were able to spatially control and shape pheromone gradients, allowing the use of a biophysical model to infer the properties of large-scale gradients generated by mating populations in a single, quantitative experimental setup, predicting that the shape of such gradients depends quantitatively on population parameters. Spatial optogenetic control of diffusible signals and their degradation provides a controllable signaling environment for engineering artificial communication and cell-fate systems in gel-embedded cell populations without the need for physical manipulation.

1. Introduction

Cell-cell communication through extracellular signals enables the spatiotemporal coordination of cell behavior across various scales, from single cells to tissues. The interplay between signal production, diffusion, and reaction (*e.g.*, internalization, adsorption, and degradation) shapes the concentration landscapes that cells experience and ultimately determines a cell's responses. A classic example is the establishment of positional information in the *Drosophila melanogaster* syncytial embryo, in which an exponentially decaying extranuclear *bicoid* morphogen gradient forms as a result of the specific location of emitter nuclei on the anterior region, free diffusion of the signal, and homogenous degradation of the signal throughout the embryo[1,2]. This smooth gradient is "read" by nuclei to switch on specific differentiation programs in sharply defined spatial locations.

In contrast to multicellular developmental systems where cells follow a predefined program from a well-defined initial condition, communication does not necessarily occur within closed spaces for free-living microbes. Populations of single cells often have a random spatial distribution, expand freely, explore an unknown environment, and create an ecosystem—the size and dynamics of which are the result of cellular metabolic interactions and cell-cell communication. As in development, signal landscapes depend on reaction-diffusion dynamics; however, population-level parameters such as cell density, population composition, and the spatial distribution of emitter and receiver cells are inherently variable in the context of single-cell populations. Thus, the way cells extract information and take appropriate decisions in such an uncertain environment is a very different biological problem than what is observed in embryology.

57 In the well-known example of mating through pheromones in the budding yeast *Saccharomyces*
58 *cerevisiae*, information gathered by cells is usually considered positional, *i.e.*, gradients formed will
59 attract cells to polarize towards the position of the source. It is generally accepted that, in nature,
60 such positional information is used by cells only over very short ("touching") distances from
61 partners[3]. This is in agreement with ecological lifestyle of *S. cerevisiae*, where mating-type
62 switching[4] and intra-ascus mating[5] , where mating cells are placed in close contact to each other,
63 ensure fast return to the diploid lifestyle.

64 The molecular mechanism underlying gradient tracking involves polarisome movement (with both
65 deterministic[6,7] and stochastic stages[8,9]) in response to pheromone-producing adjacent cells. During
66 mass mating reactions, cells display mostly such "short-range" chemotropism (**Fig. 1A**), where
67 growth and cell-body extension beyond one cell length does not occur prior to fusion. In contrast,
68 cells in microfluidic devices, subject to artificial gradients, display what we can call long-range
69 chemotropism (**Fig. 1A**), where the whole cell body extends, greatly increasing the length, cell
70 surface and volume of cells. Additionally, filamentous growth, where cells extend and bud in the
71 direction of gradients, has been observed in pheromone disc assays[10].

72 Chemotropic behaviors suggest a role for cell elongation in directed mate-finding. Such behavior
73 is potentially relevant for sparse populations generated after spore dispersal events in wild
74 yeast[11,12], where mating type switching is not the rule. Indeed, wild isolates of *S. cerevisiae* display
75 large differences in their propensity to mate or to enter the cell cycle and thus spores germinating
76 in the wild may often form microcolonies before engaging in mating[11]. Importantly, as in bacterial
77 quorum sensing[13], "demographic" information has also been shown to be a relevant cue in sparse
78 mating populations[3,14,15]. These examples highlight the idea that mating responses are not restricted

79 only to close-contact interactions in nature, and that population-parameters could be therefore
80 relevant in both natural and synthetic ecosystems.

81 Mating in yeast is governed by the mating-pheromone pathway,[16,17] which relies on the secretion
82 of pheromones to signal the presence of different mating types (*MAT***a** and *MAT*α). The *MAT***a** and
83 *MAT*α mating-types exchange pheromones to trigger activation of their mating pathway,
84 orchestrating a dedicated transcriptional program, cell cycle arrest, and morphological changes that
85 culminate with cell and diploid formation. Distinct branches of the pheromone pathway control
86 transcriptional (Ste12 branch) and arrest/morphology behaviors (Far1 branch). Dose-response
87 experiments measuring the responses of *MAT***a** cells to the purified pheromone α-factor in bulk
88 showed that, while the transcriptional branch of the pathway displays a Michaelian (linear at low
89 doses) input-output relation[18], cells transition sharply—following a Hill-type sigmoidal response—
90 from proliferating to growth-arrested elongated phenotypes (called "shmoos") characterized by
91 their mating protrusions [19,20]. This "mating switch" **(Fig. 1B)** was notably observed in artificial
92 gradients of α-factor[21,22] generated using microfluidic devices. In this setting, cell cycle-arrested
93 morphologies were observed over a narrow range of concentrations (1–5 nM) of α-factor. Cells only
94 displayed chemotropic behavior, elongating their cell body up the α-factor gradient, within this
95 concentration range. However, importantly, it remains unknown how the amplitude and steepness
96 of artificially generated gradients in the context of microfluidic devices compare to those within
97 heterogeneous, large populations of mating cells. Indeed, elongation with full accuracy of
98 elongated-cell chemotropism in microfluidic chambers is generally observed at high gradient and
99 amplitude values[9,19,21–24] (hundredths of pM/μm). Thus, the question remains: under which

100 conditions mating populations produce such specific gradients such that cells undergo useful long-
101 range chemotropism?

102 In addition to responding to α-factor, *MAT***a** cells secrete the Bar1 protein which degrades α-factor
103 extracellularly. Thus, the pheromone landscape[3] that *MAT***a** cells experience is not only determined
104 by spatiotemporal diffusion of the α-factor pheromone produced by *MAT*α cells, but also by the
105 concentration of Bar1 they produce themselves. For a non-motile organism such as *S. cerevisiae*,
106 evolution would be expected to produce systems where the concentrations of α-factor that trigger
107 mating are found only in the vicinity of emitter cells, so that cells do not have mating responses
108 unless they are very close to a partner. Bar1 has been deemed responsible to exert such a function[25],
109 by increasing the degradation rate of α-factor and confining its activity close to the producer cells,
110 consequently shortening the length-scale at which mating sensing occurs to only a few micrometers
111 (a fraction of cell size). However, in sparse, growing mating reactions, the concentration of Bar1 is
112 dependent on the density of *MAT***a** cells[14]; therefore, the levels of Bar1 may not always be sufficient
113 to degrade the α-factor produced by cells of the opposing mating type. This implies that the mating-
114 switch distance can be, in theory, extended further away from the source position (**Fig. 1C**).
115 Consequently, the superimposition of gradients produced by multiple pheromone sources
116 represents a potential confounding factor (**Fig. 1D**): partners located at a distance from source cells
117 cannot decide with which partner to mate[26]. Indeed, in mating discrimination assays[26], *bar1Δ MAT***a**
118 can discriminate real emitters from dummy (that do not produce pheromone) emitters, but only if
119 real emitters are in the minority. This suggests that in the absence of degradation, pheromone halos
120 from other cells can be a confounding factor for receiver cells. In summary, it remains unclear how

121 cells extract relevant positional information from physiological pheromone concentration
122 landscapes[3].

123 Several theories have attributed various possible functions to Bar1 in mating populations. Three of
124 these theories depend on high local concentrations of Bar1 in receiver cells, acting as a localized
125 sinks of α-factor: (i) reducing the size of the pheromone halo around emitters (at the expense of
126 gradient strength) to correctly align to gradients in the presence of multiple sources[27], (ii) gradient
127 disentanglement from two sources in close-proximity (intra-ascus) interactions,[28] and (iii) mutual-
128 avoidance in *MAT***a** cells[29]. Despite these functions requiring direct interactions of Bar1 with the cell
129 wall, a large fraction of Bar1 is considered to be widely diffusible.

130 Understanding the spatial properties of α-factor-mediated communication between mating types
131 requires characterizing the properties of physiological α-factor gradients. Although the shape of
132 gradients can be inferred using numerical simulations of cells randomly arranged in space[30], the
133 inability to experimentally control α-factor production locally and the high response variability
134 among receivers preclude the construction of predictive models. Here, we address this problem
135 using the power of optogenetics (**Fig. 1E**). We developed a method for the spatial control of α-
136 factor's production and degradation in *Saccharomyces cerevisiae* and obtained a quantitative
137 description of extracellular α-factor gradients under physiological conditions. Combined with a
138 diffusion-reaction model, we inferred quantitative parameters that describe the mating
139 communication system, providing direct quantitative support to indirectly inferred pheromone
140 gradient and response properties in a single assay. In synthesis, we provide proof of principle for
141 the optogenetic quantitative control of extracellular signal gradients within microbial cell
142 populations.

143 # 2. Results

144 **2.1 Engineered optogenetic induction of physiological range α-factor levels allows spatial**
145 **control of mating.**

146 We first aimed at engineering light-inducible strains that can produce physiological levels of
147 pheromone, by improving on a previous strain design[31]. For this we first engineered wild-type
148 *MAT*α yeast cells using a CRISPR-based promoter replacement strategy (**see Methods**) to replace
149 the promoter of the two α-factor pheromone-coding genes (MF-α1 and MF-α2) with the P_{C120}
150 promoter, the activity of which is induced by the light-sensitive transcriptional activator EL222[32].
151 Additionally, to increase α-factor production and recover wild-type levels, a second copy of the
152 P_{C120}-MFα1 construct was inserted at an unrelated locus (**Fig. 2A, Figure S1, see Methods**) to yield
153 the "opto-α" strain used in this study. To quantify the levels of α-factor produced by the opto-α
154 strain, we used a *MAT***a** reporter strain that harbors a super-folder green fluorescent protein (GFP)
155 downstream of the P_{FUS1} pheromone-responsive promoter[14] (**Fig. 2B**). This reporter strain harbors
156 the native untranslated terminal region (UTR) of FUS1 and carries a ubiquitination sequence that
157 targets super-folder GFP for faster degradation, thus providing a good estimate of the abundance
158 of the native transcript[14]. We stimulated mixes of opto-α and reporter strains with light using a
159 custom-made light-plate apparatus[33] and quantified the levels of the α-factor pheromone (relative
160 to the wild-type MATα strains) using two reporter strains that either carry or lack the Bar1 protease
161 (**Fig. 2B**).

162 In both cases, the levels of α-factor were light-intensity dependent. In the absence of Bar1,
163 pheromone levels reached the induction levels achieved by the wild type. Under the more stringent

164 conditions where receiver cells express Bar1, the opto-α strain reached up to ~60% of the wild-type
165 response. As (i) other strains and conditions resulted in lower α-factor production levels (**Fig.**
166 **S1,S2**), (ii) sample treatment of optogenetic strains puts them at disadvantage in terms of
167 pheromone production as, comparatively, wild-type cells constantly produce Bar1 during pre-
168 illumination processing (see methods), and (iii) in general mating is very robust to various
169 pheromone levels[34], we decided to focus on the opto-α strain and decided to score its wildtype
170 physiological pheromone production by checking if the levels of pheromone produced can rescue
171 wild-type physiological behavior. For this, we tested the capacity of *MAT***a**-*bar1*Δ reporter cells to
172 develop mating protrusions in response to light-induced α-factor production by opto-α cells. With
173 sufficient intensity of light and, like with wild-type *MAT*α emitters, we observed formation of
174 protrusions by *MAT***a** *bar1*Δ cells in gel-embedded mixes (**Fig. 2C, see Methods**). Finally, we
175 assayed diploid formation in opto-α/*MAT***a** mixes as a measure of the final physiological output of
176 the mating pathway (**Fig. 2 D,E**). For this, we developed an "optogenetic mating assay" (**Fig. S3,**
177 **see Methods**) based on three features. First, we used the top-agar technique to embed mating
178 mixtures (as used in classical growth arrest assays), which provides a homogeneous layer where
179 cells are located sparsely and grow as microcolonies. Second, we employed a digital micromirror
180 device (DMD)[35] to expose the cells to spatial light patterns projected into the agar (**See Methods**);
181 and finally, auxotrophic markers were used to ensure that only diploid colonies can grow, allowing
182 us to have a measure of light-induced mating efficiency. Our results show that pheromone
183 production is indeed sufficient to induce cell-cell fusion with wild-type *MAT***a** in a light dose-
184 dependent manner and could reach comparable maximum levels as the wild-type *MAT*α emitter
185 (**Fig. 2 C,D**).

186 Taken together, these results show that the opto-α strain is a suitable candidate, comparable to the
187 wild-type, that produces physiological-range levels of pheromone production and mating behavior
188 in response to light. Therefore, we employed the opto-α strain as a remotely controlled signal
189 generator to create realistic α-factor spatial gradients within large populations of opto-α/MATa
190 cells.

191 **2.2 Optogenetic induction of pheromone degradation allows specific control of growth.**

192 It is expected that both pheromone production and pheromone degradation by the α-factor
193 protease Bar1 shape extracellular pheromone gradients[30]. To gain spatial control over pheromone
194 degradation, we constructed the opto-Bar1 *MAT***a** strain, in which the α-factor protease Bar1
195 expression is placed under control of the P_{C120} light-inducible promoter. We followed a similar
196 promoter replacement strategy as for the opto-α strain, targeting the Bar1 locus in *MAT***a** cells (**Fig.**
197 **3A**). The expression levels and activity of Bar1 protein were measured using the *MAT***a** *bar1*Δ α-
198 factor reporter, in the presence of purified α-factor added to the media. The levels of GFP produced
199 by the reporter strain were used to quantify the production of Bar1, since Bar1 degrades purified
200 α-factor in the culture medium (**Fig. 3A**). We observed light-dependent Bar1 activity, with the level
201 of the reporter response decreasing as the light intensity increased (**Fig. 3B**). We reached higher
202 Bar1 activity than the wild-type strain and undetectable basal (in the dark) Bar1 enzymatic activity.

203 Although Bar1 degrades the pheromone, its function has been long associated with increases in
204 mating efficiency through several candidate mechanisms[14,26–29] (see **Introduction**). However, the
205 presence of Bar1 is not essential for mating itself. Indeed, when performing the optogenetic mating
206 assay with the opto-Bar1 strain, cells located in dark regions—where *MAT***a** cells do not express
207 Bar1—remain proficient at forming diploids (**Fig. 3C**), with a ~2-fold difference in mating efficiency

208 between illuminated and dark regions (**Fig. S4**). Thus, contrary to optogenetic pheromone
209 induction—and as expected—optogenetic pheromone degradation does not restrict but mildly
210 enhances the final output of the pathway, namely the formation of diploids.

211 Cell cycle arrest, another physiological output of mating events, is controlled by the mating-
212 pheromone pathway through the FAR1 branch[36]. When Bar1 is produced and actively degrades α-
213 factor, one would expect to observe fewer cell cycle arrest events. Following similar methods as for
214 diploid formation, we used the optogenetic plate assay to measure the capacity of *MAT***a** cells to
215 escape cell cycle arrest as a function of Bar1 induction. We imaged an intermediate stage of the
216 experiment (**Fig. 3D**). A differential growth pattern was observed in the non-selective plate used as
217 template for replica plating in diploid-selective media (See also **Fig. S3**), as illuminated cells
218 (expressing Bar1) grew similarly to wild-type levels, whereas non-illuminated cells did not grow
219 significantly (**Fig. 3D-F).**

220 These results show that illuminated opto-bar1 cells recover the expected wild-type behavior in
221 terms of α-factor degradation activity, mating, and proliferation. They also show that Bar1 is an
222 effective spatial growth control actuator for synthetic biology applications.

223 **2.3 Spatial optogenetic induction of α-factor production generates distance-dependent**
224 **responses in mating populations.**

225 After quantitative characterization of our optogenetic strains, we next moved to assess the spatial
226 properties of pheromone-mediated communication between *MAT*$\boldsymbol{\alpha}$ and *MAT***a** cells in an idealized
227 (but physiological) context. To that end, we implemented the "half-domain assay", which consists
228 of monitoring *MAT*α/*MAT***a** mating reactions within a spatially homogeneous random distribution

229 of cells of both mating types placed at the bottom of agarose-embedded "miniwells" (**Fig. 4A, see**
230 **Methods**). Half of the total surface was exposed to blue light, to optogenetically induce pheromone
231 production exclusively in the illuminated domain. The response of reporter cells along the axis
232 perpendicular to the light-dark border allowed us to read and quantify the diffusion-reaction
233 properties of α-factor.

234 We first conducted experiments with the opto-α strain as a light-dependent pheromone generator
235 and the *bar1Δ MAT***a** reporter strain as a pheromone receiver and fluorescent reporter of mating
236 behavior. Absence of Bar1 simulates natural situations where wild-type *MAT***a** receivers are in the
237 minority (*e.g.*, upon a mating type switching event), where Bar1 levels are not enough to modify
238 the global pheromone concentration. Thus, in this experiment, enzymatic degradation of α-factor
239 by Bar1 is absent and disappearance of the pheromone is solely determined by its intake by cells[37].
240 After illumination (**See Methods**), cells along a stripe located in the center of the plate, with its long
241 axis perpendicular to the light-dark interface, were imaged (**Fig. 4B)**. A schematic of the experiment
242 and strains used is also shown (**Fig. 4C**). The opto-α strain was equipped with a red nuclear marker
243 (the HTB2 histone fused to mApple) for easy identification, which is especially important in regions
244 of clumping (**Fig. S5**, this new strain is named opto-α*). We used a 20x objective and an automated
245 stitching method (**see Methods**) to obtain images of a large stripe (5671 μm x 330 μm) of both cell
246 types using fluorescence and bright field microscopy at single-cell resolution (**Fig. S5**). Our
247 experimental results revealed a sharp phenotypic transition between illuminated and non-
248 illuminated areas. The sharpness of this transition (compared to the sharpness of the light border)
249 was assessed by running a parallel experiment in neighboring mini-wells by stimulating a control
250 strain that expresses YFP under the control of an equivalent EL222/P_{C120} light-inducible system. This

control serves as a biological spatial imprint of the light-stimulated region, to both locate the position of the border in the sample and determine the sharpness of the light border (**Fig. 4D,E**). The region in the vicinity of the light-to-dark transition border illustrates the overall trend of the mating response in the *MAT***a** *bar1*Δ responder population: the GFP signal gradually vanished in cells further and further away from the frontier in the dark domain (**Fig. 4D**). Importantly, since we imaged cells at single-cell resolution, we clearly observed the cell morphology transitioned from elongated shapes to round as the distance from the light to dark frontier increased (**Fig. 4E**).

Our assay demonstrates that optogenetics can be used to produce large-scale population-generated gradients of a pheromone to infer the shape of the pheromone gradient through quantification of gene-expression and cell-morphology outputs (**Figs. 4C,D, S5).**

2.4 Biophysical modeling reveals a quantitative dependency of large-scale gradient shape on population-parameters

Using the half-domain assay, we next sought to infer the biophysical properties of the generated gradient. Thus, we constructed a biophysical model based on reaction-diffusion dynamics—as well as dose-response functions—and obtained single-cell quantifications of pheromone-responses using a combination of manual and automated single-cell segmentation and analysis (**see Methods**). We investigate what equation governs the time (t) evolution for the concentration of α-factor $c(x, z, t)$ as a function of the position relative to the frontier of the dark domain (x, with the frontier at $x = 0$) and the distance from the glass surface (z, with the glass surface at $z = 0$). Pheromone-producing cells are located on the glass surface in our experiment, while pheromones diffuse into the agarose gel volume sitting on top of the cells (see **Fig. 5A**). Further, since we know

that pheromone degradation happens mainly by cell uptake[37] in a Bar1 knockout, degradation can happen only on the boundary close to the glass surface:

$$\frac{\partial c(x,z,t)}{\partial t} = \mathrm{D}\nabla^2 c(x,z,t) + r\rho_\alpha \delta(z)\Theta(-x) - \Omega\rho_A \delta(z) c(x,z,t), \quad (1)$$

which depends on its diffusion coefficient D, the cell surface density ρ_α and ρ_A respectively for *MAT*α and *MAT***a** cells, the pheromone production rate per cell r, and a parameter proportional to the rate of degradation of the pheromone per cell Ω, which has units of rate times length cubed. We analyze Ω further in the **Supplementary Information**. As an approximation, we assumed these parameters to be time-independent.

The solution to Eq. 1 at steady state is derived and plotted in **Supplementary Information,** the concentration is highest on the production domain far from the boundary and lowest on the diffusion domain symmetrically. The transition is logistic-like (**Fig. 5B**) and centered on the boundary, it is sharper closer to the glass surface and gradually smoother for larger values of z (see **Supplementary Information**). The precise shape of the transition depends on the finite size of the definition domain, specifically it depends on the length of the glass plate stripe L_x and the thickness of the agar volume sitting on top of the cells L_z. Apart from these, the solution depends on a single length scale $\lambda_\alpha \equiv \mathrm{D}/(\Omega\rho_A)$ defined by the rate between the diffusion and degradation rate density at the surface. In the large domain limit ($L_x \gg \lambda_\alpha$ and $L_z \gg \lambda_\alpha$) the finite size effects are negligible and the solution simplifies significantly. On the glass surface ($z = 0$) where the cells are located, the

concentration is directly proportional to the ratio between production and degradation rates and can be described by following closed formula:

$$c(x) = \frac{r\rho_\alpha}{\Omega\rho_A}\left[\Theta(-x) + \frac{\cos\left(\frac{x}{\lambda_\alpha}\right)}{\pi}\operatorname{sign}(x)\left(\frac{\pi}{2} - \operatorname{Si}\left(\frac{|x|}{\lambda_\alpha}\right)\right) + \frac{\sin\left(\frac{x}{\lambda_\alpha}\right)}{\pi}\operatorname{Ci}\left(\frac{|x|}{\lambda_\alpha}\right)\right], \qquad (2)$$

where $\Theta(x)$ and $\operatorname{sign}(x)$ are respectively the step function and the sign of its argument while $\operatorname{Ci}(x)$ and $\operatorname{Si}(x)$ are the trigonometric integrals functions. While Eq. 2 is logistic-like in shape, it features a heavy tailed decay of the gradients (as $c(x) \propto \lambda_\alpha/x$) for large distances from the light boundary ($x \gg \lambda_\alpha$), in sharp contrast to systems traditionally modelled in one-dimension—such as the drosophila embryo—where decays are exponential. The concentration at the boundary $c(0) = r\rho_\alpha/(2\Omega\rho_A)$ depends on the rates of emission and absorption as well as the surface density of emitter and absorbing cells. On the glass surface in this half domain essay, we expect densities of α-factor much greater than the one obtainable for a single cell-source, since the density of producers is greater than one cell within one decay length of the observed profiles ($\rho_\alpha > 1/{\lambda_\alpha}^2$).

To connect these analytical results to the experiments, the response $\theta(x)$ of the mating pheromone pathway to the steady-state concentration of pheromone is modeled by composing the result for $c(x)$ with a Hill function with coefficient n. This results in:

$$\theta(x) = \frac{1}{1 + \left[C \cdot \frac{c(x)}{2c(0)}\right]^{-n}}, \qquad (3)$$

309 where $C \equiv 2c(0)/\mathrm{EC}_{50}$ is the concentration of the ligand far away from the border ($x \to -\infty$)
310 in "EC_{50}" units, namely, the concentration producing the half-maximal P_{FUS1} mediated gene-
311 expression response. We obtained the theoretical shape for a standard concentration profile at
312 various values of C and two different values of n **(Fig. 5C,D)**. It is well known that no cooperativity
313 is involved in the gene expression output from the P_{FUS1} promoter[14], we thus fixed $n = 1$ for gene
314 expression output. Experimental responses are measured in unknown concentration units and are
315 affected by a baseline that needs to be determined, for this reason we fit the experimental data to a
316 formula that takes into account these two extra parameters $\hat{\theta}(x) = A \cdot \theta(x) + b$. It is important to
317 note that the Hill-equations saturate at very large concentrations ($C \gg \mathrm{EC}_{50}$), while in all our
318 experiments we determined C (the pheromone concentration at the curve's plateau) to be of the
319 same order of magnitude as its EC_{50}, *i.e.* the response curve becomes flat far from the border in the
320 left domain because of a constant concentration of pheromone, and not because of saturation (see
321 Section 2.5 below). We were able to fit independently both the normalization parameter A as well
322 as the ligand concentration far away from the border C thanks to the availability of two readouts
323 of the pheromone concentration with different Hill coefficients n.

324 **2.5 Quantitative analysis reveals that population-level pheromone gradients are long-range,**
325 **shallow, and limit morphological transitions to the vicinity of the source.**

326 Armed with the model derived in the previous section, we quantified the single-cell outputs of the
327 activity of the mating pheromone pathway—specifically, P_{FUS1} dependent gene-expression (**Fig. 5E**;
328 determined using standard illumination correction and segmentation tools; **see Methods**) and cell
329 elongation (**Fig. 5F**; determined independently and manually; **see Methods**)—in *MAT***a** cells
330 lacking Bar1. Our results revealed a gradient of fluorescence intensity that extends far beyond the

331 region where the pheromone is generated (**Fig. 5E**). Thus, the transport properties of α-factor can
332 generate responses at distances spanning hundreds of cell lengths, consistent with a widely
333 diffusible molecule. The morphological transition (**Fig. 5F**) is steeper than the gene expression
334 response, with cells increasing their maximal length within a narrower distance range and at a
335 higher pheromone concentration. This is expected, as the morphological transition is indeed
336 switch-like[18,20].

337 We ran control experiments using (i) opto-α emitters mixed with the wild-type *MAT***a** reporter
338 (expressing Bar1) and (ii) a mixture of the wild-type *MAT*α as light-independent emitters and the
339 *MAT***a** *bar1Δ* reporter. To ease cell segmentation, we performed a machine-learning based protocol
340 (See methods) to obtain a global picture of the behavior of both samples and controls. In the reaction
341 with wild-type expression of Bar1, basal GFP output was obtained with no detectable differences
342 between the light and the dark domains. In contrast, in the mix with wild-type *MAT*α and the
343 *MAT***a** *bar1Δ* reporter, strong activation was observed in both illuminated and dark domains (**Fig.**
344 **S6**). These controls further allowed us to compare the maximum GFP output activation of the opto-
345 α and wild-type *MAT*α strains to confirm that the emission levels are close to physiological in the
346 half-domain assay, as well as allowing us to correct illumination inhomogeneities and background-
347 bleaching effects of light induction with an independent method (**Fig. S6, see Methods**).

348 We also observed that cells elongate, but do not preferentially grow towards (nor away from) the
349 large-scale gradient, as revealed by the lack of enrichment of cells with orientations close to 0° or
350 180° respect to the direction of the gradient (**Fig. 5F, inset**), demonstrating that—even at its steepest
351 point (the border)—the large-scale gradient is insufficient to induce chemotropism. In addition,
352 because we did not observe formation of single or multiple "thin protrusions", characteristic of

353 saturation of the pheromone pathway and observed in our reporter[14,19,38], we concluded that cell
354 responses lie within the sensitive range of the pathway, which is indicative of the Ste2 receptor not
355 being saturated.

356 Next, we used the biophysical model (**see Supplementary information**) to infer key quantitative
357 parameters of the gradient. We fitted the experimental datapoints for the two observables to $\hat{\theta}(x)$
358 (**Fig. S7**), with n fixed to one for the gene expression output (**see Methods**), and fits displayed on
359 top of the raw rather than the normalized data (**Fig. 5E,F**). In this way, we inferred the basic
360 properties of the gradients generated (**Fig. 5G**): the best fit returned us the steady-state decay length
361 $\lambda_\alpha \sim 735$ μm, the steady state concentration of α-factor for $x \ll -\lambda_\alpha$, $C = 1.45\ \mathrm{EC}_{50}$, and the Hill
362 coefficient of the morphological response ($n = 3$). The gradient value at light-dark transition
363 border, the expected steepest point of the large-scale gradient, has a value of ~ $5 \cdot 10^{-3}\ \mathrm{EC}_{50}/\mu\mathrm{m}$.
364 Using an EC_{50} value for the response of 1–3 nM[14,18,19], we obtain a value of 5 to 25 pM/μm or, roughly,
365 ~70 pM per cell diameter (one cell diameter is ~5μm). Such shallow gradients will produce
366 differences in receptor occupancy between each side of the cell below the minimal ~0.5% observed
367 in chemotropic cells in artificial pheromone gradients[39].

368 Collectively, these results imply—in this spatial arrangement and in the absence of Bar1—that: *(i)*
369 pheromone levels characteristically decay roughly ~100 cell bodies away from producer regions or
370 single cells; *(ii)* maximal steady-state pheromone levels found in typical (dense but not crowded)
371 mating populations are not saturating and rather very similar (less than double) to the EC_{50} of the
372 response (its most sensitive point); *(iii)* cells "ignore" (filter out) large-scale gradients (such as those
373 produced within the spatial limit of finite emitter populations) that are non-informative about the
374 location of nearby emitters; and *(iv)* knowing the dependency of pheromone concentration at the

375 border on the linear density of cells (~100 cells/mm or ~70 cells in one decay length), $C/2$ would be
376 reduced by around two orders of magnitude for a single cell located at the border. This means that
377 for a single cell, pheromone levels close to the EC_{50} cannot be reached, even in its immediate
378 vicinity. This is consistent with the need for close-proximity mechanisms and focal pheromone
379 emission[9] for such close-contact situations. In other words, single emitters cannot induce elongation
380 or chemotropism in responding cells, even in the absence of Bar1. Sufficient pheromone levels to
381 induce mating behavior at a distance are always produced by a collective of cells and under low
382 Bar1 conditions (biased ratios). Increased rates of degradation of the pheromone (*e.g.*, in the
383 presence of *MAT***a**-bound Bar1) would scale down the gradient. These constraints over the
384 maximum levels of pheromone that a single cell can produce might explain why—when
385 homogeneous Bar1 sources are present—we did not observe elongation in either of the two
386 domains (**Fig. S6**) and the response values stayed at basal levels, despite the high density of
387 emitters.

388 **2.6 Quantitative analysis of large-scale gradients produced by opto-Bar1 receivers suggests**
389 **localization of Bar1 activity in its production domain.**

390 Our experiments in the absence of Bar1 are adequate to explain natural situations where wild-type
391 *MAT***a** receivers are in the minority (*e.g.*, upon a mating type switching event), such that Bar1 is not
392 abundant enough to modify the large-scale pheromone landscape. As the mating-type ratio
393 becomes unbiased, *MAT***a**-produced Bar1 protease becomes important. When mated under
394 conditions of pure diffusion-reaction—but not advection—Bar1 is believed to allow reshaping of
395 the pheromone landscape. The exact nature and biological function of this reshaping activity

396 during mating remains controversial[3]. Therefore, we used the half-domain assay with the opto-
397 Bar1 strain in the presence of wild-type MATα cells as emitters to shed light on the problem.

398 In this case, WT pheromone production is homogeneously distributed on the glass surface and
399 emission of Bar1 is localized in one half-domain of the glass surface (**Fig. 6A**), on the right of the
400 light-dark transition border (**Fig. 6A, Fig. S8**). For this assay, wild-type *MAT*α emitter cells were
401 tagged with a green nuclear tag, while opto-Bar1 cells were tagged with a red nuclear tag. This
402 allowed us to confirm that, as in the Petri dish experiments (**Fig. 3D-F**, **Fig. S4**), mating events
403 (measured as nuclei fusion events) happen in both illuminated and non-illuminated areas and that
404 Bar1-mediated increases in mating events correlate with the increased initial growth of *MAT***a** (**Fig.**
405 **S9**). Crucially, observations of the cell-elongation phenotype revealed a striking difference
406 compared to this response's profile in the opto-α experiment (**Fig. 5)**: in the opto-Bar1 case, the
407 elongation pattern emerges far away from the border, well into the dark (left) region of the
408 experiment (**Fig. 6B-C**).

409 To understand the observation we turned to modeling, and—as a simplification—we solved the
410 Bar1 production domain acting as a perfect sink for α-factor model. In this configuration, Bar1 is
411 confined to the glass surface in the production domain ($z = 0,\ x > 0$) and the α-factor degradation
412 rate by Bar1 is set so high that it effectively degrades all α-factor in its presence. These limits lend
413 themselves to a simple change in boundary conditions at $z = 0$, for the diffusion of α-factor, respect
414 to Eq. 1 (derivations and detailed solution **Supplementary Information**). Similarly to what has
415 been used to obtain Eq .2, in the infinite domain limit the profile for α-factor concentration on the
416 glass domain follows the following:

$$c(x) = \frac{r\rho_\alpha}{\Omega\rho_A}\left[\Theta(-x) + \frac{\cos\left(\frac{x}{\lambda_\alpha}\right)}{\pi}\mathrm{sign}(x)\left(\frac{\pi}{2} - \mathrm{Si}\left(\frac{|x|}{\lambda_\alpha}\right)\right) + \frac{\sin\left(\frac{x}{\lambda_\alpha}\right)}{\pi}\mathrm{Ci}\left(\frac{|x|}{\lambda_\alpha}\right)\right]. \quad (5)$$

Even if α-factor is produced on the full glass plate (*vs.* Eq. 2 where α-factor is produced only on a half domain), due to the high efficiency of Bar1 in degrading α-factor (*vs.* Eq. 2 where α-factor is degraded by cell intake), in Eq. 5, $c(x)$ is exactly equal to zero over the full Bar1 production domain. Further, due to the confinement of Bar1 on the glass surface of the producing domain, $c(x)$ quickly increases on the diffusion domain with a slope that is set by the same λ_α that has been measured in the experiment without any Bar1. Finally, for the same reason, the concentration far from the boundary $\frac{r\rho_\alpha}{\Omega\rho_A}$ as well as the Hill coefficient n, the baseline B and the arbitrary unit A, in the α-factor concentration dependent cell response function $\hat{\theta}(x)$ are predicted to be the same as in the experiment without any Bar1. Considering this, we overlapped the predicted cell response function for elongation $\hat{\theta}(x)$, using the solution to Eq. 5 for the α-factor concentration, to the experimental data in presence of Bar1, fixing all the parameters using the ones fitted to the experiments in absence of Bar1 presented in the previous section (*i.e.* with zero free parameters) and obtained a reasonable agreement to experimental data (**Fig. 6C**). This indicates that Bar1 is efficient in degrading α-factor respect to cell intake, and that its diffusion is compatible with localization on the glass domain in the production domain. Further, if we allowed in the equations for Bar1 to diffuse substantially in the agar volume above the producing cell, due to the long range nature of diffusion in our geometry, and the progressive flattening up of the gradients above the glass surface (see Eq. 2), Bar1 would have penetrated substantially in the diffusion domain and it would have degraded α-factor there substantially reducing the cellular response respect to the experiment without Bar1. Considering that this didn't happen, we conclude that Bar1 penetration is limited.

438 # 3. Discussion

439 Using our optogenetic tool, here we show that in sparse yeast populations, biologically relevant
440 concentrations of α-factor in the environment are built up by the contributions of many emitter
441 cells, and that there is a length-scale for gradient formation other than that in the well-known
442 immediate vicinity of cells (1 cell body or ~5 μm); namely, the large-scale gradient formed at the
443 edge of finite producer populations. Chemotropism directed along these collectively generated
444 large-scale gradients was not observed in our half-domain assays. These large-scale gradients are
445 thus not steep enough to induce chemotropism, despite pheromone concentrations being high
446 enough to trigger strong elongation. Then, *MAT***a** cells filter out these uninformative large-scale
447 gradients and rather only follow local gradients with sufficient steepness[9]. Elongation responses in
448 this case better resembles random rather than active search for mates.

449 Our model confirms previous calculations[8] showing that concentrations of pheromone emanating
450 from a single emitter must be well below the mating threshold (**Fig 5H**), this means that pheromone
451 secretion by a single cell doesn't generate meaningful long-range gradients that can be followed
452 with chemotropism involving cell elongation—even if partners are sensitized (without expressing
453 Bar1). Long-range gradients are therefore only collectively produced in mating reactions. Indeed,
454 compared to values generating long-range chemotropism in microfluidic devices, large scale
455 gradients in the half-domain assays are roughly ~10x shallower (we report ~5 to 25 pM/μm whereas
456 in studies with precise quantification of the gradients generated, these are in the order of
457 hundredths of pM/μm[19,40]). We expect very similar behavior for wild type α-factor emitter, because
458 the pheromone production rates are comparatively very similar.

459 Our results also show that Bar1 effectively tends to stay in its production domain. It is possible that
460 such behavior comes from out-of-steady-state effects. Namely, that both pheromone and Bar1
461 diffuse widely, but that Bar1, due to its size, does so slower. Taking the values for diffusion from
462 earlier simulation work[30] we get half a millimeter diffusion on the timescale of early cell responses
463 (45 minutes), which is ballpark compatible with our observations of a shift of the boundary into the
464 left domain. On the other hand, it is well known that Bar1 is an abundant disulfide-bridged
465 mannoprotein present in the cell wall of *MAT***a** cells[41] and this sink character is essential to build
466 models that explain the establishment of gradient disentanglement from two sources in close-
467 proximity intra-ascus interactions[28] and mutual-avoidance in *MAT***a** cells[29]. Simulation work has
468 either introduce high bulk degradation of Bar1[29] or zero-diffusion of Bar1 to keep Bar1 halos
469 localized to emitter cells. Considering the clear evidence for Bar1 association with cell walls and
470 the lack of evidence for specific Bar1 degradation, the latter alternative—added to slower diffusion
471 for the freely diffusible Bar1—seems the most likely explanation. More experimentation is needed
472 to elucidate the precise mobility of Bar1 during mating.

473 In any case, such limited diffusion of Bar1 does not prevent *MAT***a** from modifying global
474 pheromone profiles—provided cells are at a sufficient cell density. Indeed, in our opto-Bar1
475 experiment (**Fig. 6A-C**), Bar1 greatly reduces the global α-factor concentration, and *MAT***a** cells do
476 not elongate nor arrest (**Fig S6**). Despite this, cells in close contact still mate normally (**Fig. S9**).
477 Thus, when separated in space, cells cannot reach the threshold for executing the morphological
478 transition. This is in agreement with the absence of elongation and the persistence of cell division
479 by *MAT***a** cells in unbiased mating reactions in the presence of advection[15]. In this sub-threshold
480 case, it is likely that increased cell-number, randomly oriented bipolar budding[10,15] and close-

481 contact mechanisms[9,42] aid mating. These known mechanisms are functionally very different as
482 search strategies to what we here call long-range chemotropism, a biological function first inferred
483 from the classical experiments by Segall in the early 1990s[24], in which cell-cycle arrested cells in
484 agarose extend their cell bodies towards a glass pipet that releases pheromone. This type of
485 chemotropism, involving cell elongation, is only accurate at concentrations matching those at
486 which cells switch[43–46]. Therefore, gradients need to fulfill two conditions to induce this behavior:
487 they must have a high mean pheromone concentration to induce elongation and need to be steep
488 enough to direct the polarisome towards the source. Our results suggest that—in mating reactions
489 with cell densities that would render chemotropic cell elongation useful—there is a trade-off
490 between the mean pheromone concentration and the steepness of the gradient: cells are weak
491 producers but, in principle, good position signalers, whereas dense populations are strong
492 signalers but weak position signalers.

493 Thus, our results explain why elongated *MAT***a** chemotropism is rarely observed as directed mate-
494 searching in mating reactions with sparse populations. Indeed, depending on the levels of Bar1,
495 within environments crowded with α-factor emitters, cells will either restrict pheromone levels to
496 the emitter vicinity and rely on local (short-range chemotropism) mechanisms[9,42] or exhibit
497 randomly oriented elongation due to gradient overlapping. Randomly oriented cell elongation
498 could be a useful strategy under such low Bar1 conditions, as gradient overlapping will make the
499 switch concentration proportional to the cell density of partners, rather than their distances. Our
500 results reveal that gradient overlapping is significant in the absence of Bar1, implying that distance-
501 to-source measurements by cells in the production region cannot be disentangled from
502 demographic (population-parameter) measurements**.** Therefore, our results highlight a limitation

503 of long-range chemotropism as an efficient mate-directed search strategy; namely, the necessity of
504 the *MAT*α-biased ratios for *MAT***a** to reach its switching threshold entails an increased likelihood
505 of producing local, uninformative gradients caused by increased overlapping. This trade-off, in
506 principle, could be balanced at some specific ratio, where Bar1 levels are enough to spatially restrict
507 levels of α-factor and sources are clustered to allow a high local concentration of α-factor. This
508 could be the case, for example, for a larger patch of *MAT*α encountering a close smaller patch of
509 *MAT***a** after mating-type switching[4], spore dispersal in wild isolates with delayed mating
510 interest[12,47], or ordered seeding for patterning applications[48,49].

511 Overall, our results suggest that the pheromone landscapes in sparse mating reactions are directly
512 shaped by population parameters and differential diffusion of Bar1 and α-factor observations.
513 Functionally, steep gradients localized at either the source or the sink can only guide chemotropism
514 when the population ratios are biased enough to limit global Bar1 availability. As suggested by
515 others, due to its sink function, the gradients might be steeper at a receiver cell; thus, if several
516 receiver cells cluster, the gradients can direct these cells away from each other[29]. Thus, gradients
517 can effectively provide information about the location of competitors (other *MAT***a** cells) rather than
518 potential mates (*MAT*α cells). In addition, local degradation of α-factor allows the asexual
519 proliferation of unmated individuals, maximizing the total population's fitness.

520 We expect our optogenetic tools to be useful to prove the limits of successful chemotropism—where
521 cells fuse—in microfluidic confinement of small groups of cells and/or microcolonies stimulated
522 with high spatial illumination resolution. In the same context, controlling dynamically (taking
523 advantage of EL222's reversibility[50]) the levels of Bar1 and pheromones (eventually including a-
524 factor optogenetic control), in confinement, could allow a deeper quantitative understanding and

525 controllability of mate search (and self-avoidance[51]). Controlling cell-cell fusion precisely in space
526 could be also useful in the context of engineered living materials[52]

527 Our study encourages the use of the yeast mating system as a quantitative framework for the design
528 and control of spatial behavior of natural and synthetic cell-cell communication systems.

529 # 4. Methods

530 All materials described here and in the Supplementary Information are available upon reasonable
531 request. Datasets used to generate the figures and the code for the mathematical modeling can be
532 found on the public Zenodo archive 10.5281/zenodo.10572403

533 **4.1 Strains and growth conditions**

534 *S. cerevisiae* strains used in this study (**Supplementary Table 1**) are derivatives of BY4741 (*MAT***a**
535 *his3Δ1 leu2Δ0 met15Δ0*), BY4742 (MATα, *lys2Δ0,* otherwise identical to BY4741), SEY6210a[53] (*MAT***a**
536 *leu2-3,112 ura3-52 his3Δ200 trp1Δ901 lys2-801 suc2Δ9*), and SEY6210 (MATα, otherwise identical to
537 SEY6210a). Yeast cells were routinely grown on complete medium (Yeast peptone dextrose; YPD,
538 Sigma) or synthetic complete (SC) medium—composed of 6.7 g Yeast Nitrogen Base without amino
539 acids (Difco 291940) and 0.8 g complete supplement mixture drop-out (Formedium DCS0019) in 1
540 L—supplemented with 2% glucose (Merck). Cells from glycerol stocks or agar plates were
541 inoculated into YPD and incubated at 30°C on an orbital shaker at 250 rpm (in an Innova 4230
542 incubator) for 12 to 16 h. Day cultures were performed by inoculating 5 mL of SC or YPD media

543 with overnight cultures at a concentration of 1% *v/v*. Care was taken to reduce unwanted light
544 exposure as much as possible before the start of the experiments by covering the agar plates and

545 precultures in aluminum foil and by performing all steps without direct exposure to light (low
546 ambient light).

547 All yeast transformations were conducted following a standard lithium acetate protocol. To replace
548 the native promoters located upstream of the genes of interest with the EL222-dependent promoter
549 P_{C120}, we performed CRISPR/Cas9-based genome editing following a method described
550 previously[54]. Oligonucleotides used in this study are listed in **Supplementary Table 2**. The
551 replacement fragments used to exchange the upstream region of the relevant genes (pheromones
552 or Bar1) were amplified from plasmid pYTK097, which contains the original sequence of the wild-
553 type P_{C120} promoter from *Erythrobacter litoralis*[55], using primers containing appropriate homology
554 regions as overhangs. DNA sequences coding for guide-RNA (gRNA) sequences (obtained from
555 IDT) used to target Cas9 to the desired loci are also listed in **Supplementary Table 2**. Short and
556 long gRNA were hybridized with each other and ligated into plasmid pML104, which possesses a
557 *Cas9* expression cassette and an URA3 marker for auxotrophic selection. The EL222 transcription
558 factor was inserted at the HIS3 locus by digesting plasmid pEZ-L105[56] with the *SfiI* restriction
559 enzyme. In this construct, EL222 is expressed from the constitutive P_{pgk1} promoter. Nuclear tagging
560 was performed by inserting mApple at the HTB2 locus by amplifying mApple from plasmid
561 pPH330 using primers oPH_0386 and oPH_0387 followed by transformation and selection using
562 G418 antibiotic selection. Nuclear tagging with mVenus was performed by replacing mApple in
563 the strain above using CRISPR/Cas9. The mVenus fragment was amplified from plasmid pPH_086
564 using the same oPH_0944 and oPH_0945 primers and guideRNAs oPH_941 and oPH_942.

565 **4.3 Light stimulation experiments in 24-well-plates**

566 Overnight cultures were diluted 1:50 in fresh LoFlo-SC (synthetic complete media prepared with
567 "low fluorescence" yeast nitrogen base lacking folic acid and riboflavin; Formedium) to reduce
568 media fluorescence and grown to an optical density (OD_{600}) of 0.4–0.5. Individual day cultures of
569 optogenetic and reporter strains were washed once with 1 volume of LoFlo-SC media, resuspended
570 to an OD of 0.5, mixed at a 1:1 ratio, and placed in black glass-bottom 24-well plates (CellVis). Light
571 stimulation was performed in a custom-made light plate apparatus based on the design by
572 Gerhardt et al[33] equipped with a blue LED (λ=461 nm). The final volume in all experiments was 1
573 mL and the incubation time was 2 h. When opto-Bar1 was used as a test strain, α-factor (Sigma)
574 was added at a final concentration of 1 μM. A well containing only the reporter strain was routinely
575 included to calculate the basal GFP expression from the P_{C120} promoter. Light intensity calibration
576 of the apparatus was performed as reported before[33] using a power-meter and a custom 3D-printed
577 adaptor. Reporter gene expression was analyzed by flow cytometry immediately after sampling.

578 **4.4 Patterned light stimulation in Petri plates**

579 Day cultures in SD media containing all amino acids were inoculated at 4% *v/v* with an overnight
580 culture and grown until the OD_{600} was ~1.0The cultures were then centrifuged at 3500 rpm for 7
581 min, the supernatant removed, the pellets washed once in SD medium containing all amino acids,
582 and the optical density adjusted to OD_{600} =1.0. These suspensions were mixed at a 1:1 ratio and 150
583 μL was added to 6 mL of 0.5% agar ("top" agar, kept in a water bath at 55°C).

584 For the "velvet" version of the assay (**Figs. 3, S4, S5**), the top agar was poured over Petri plates
585 containing solid SC-agar (1.5% agar; 20 mL total volume) supplemented with all amino acids., using
586 a leveling surface. Plates were then sealed with parafilm, keeping the lids of the plates slightly
587 tilted. Blue light patterning was performed with a DMD projector (DLP® LightCrafter™ 4500

588 TexasInstrument) placed inside an incubator (Memmert UF160); the projector projects light of the
589 desired shape and intensity over Petri plates placed over a black surface. After light stimulation,
590 the plates were replicated on SD plates lacking methionine and lysine using the sterile velvet
591 technique, incubated for at least 24 h at 30°C, and imaged using a multi-imager (Biorad) for colony
592 counting.

593 For the "direct" version of the assay (**Figs. 2, S4, S6**), agar cell suspension was poured over 20 mL
594 of 1.5% agar SD media with low lysin levels (0.005 g/L) and was directly recovered for imaging and
595 colony counting after at least 24 h of incubation (**Fig. S4**). The basis for this simpler version of the
596 assay relies on the following: because the *MAT*a and *MATα* wild-type strains are auxotrophic for
597 methionine and lysine, respectively (**See Supplementary Table 1**), we expected haploid growth—
598 and presumably mating—to depend on supplementation of these amino acids. Consequently, a
599 low concentration of these amino acids would allow mating, but later only select for diploid growth
600 as these amino acids become exhausted. We note that the methionine levels in the 150 μL cell mixes
601 are enough to allow mating, as adding methionine did not increase diploid growth. On the
602 contrary, lysine levels were optimized to determine the final concentration used (levels higher than
603 0.005 g/L did not affect diploid growth). Calibration of the light intensity of the device was
604 performed by placing a power meter at the location of the agar surface. For the determination of
605 growth levels, we used the *radial profile plot* function of Fiji, where the intensity at any given distance
606 from the central point represents the sum of the pixel values around a circle (**Fig. 3F**, inset). Such
607 integrated intensity is divided by the number of pixels in the circle, yielding normalized
608 comparable values.

609 **4.5 Half-domain gradient generation assay**

610 Rows of wells in glass-bottom 24-well plates (CellVis) were taped in the "row" direction following
611 available marks in the frame that coincide with the hemisphere of the wells. Longitudinal sections
612 of black tape were cut and the uncut side of the tape was gently positioned facing the hemisphere
613 of the wells. Overnight cultures were reinoculated at 2% *v/v* in YPD. These day cultures were grown
614 for 4 h, washed once in 4 mL of synthetic complete media with 2% glc (SC-GLC), and then
615 resuspended in 1 mL of the same media. The OD600 was determined in a cuvette benchtop
616 spectrophotometer using 100 μL of this culture and 900 μL of SD-glc. Cultures were diluted back
617 to OD_{600}=0.1 in a final volume of 5 mL **SC-glc**. Concanavalin A coating was performed as follows:
618 wells were exposed to 300 μL of 0.2 mg/mL Concanavalin A (ConA, Sigma; 1/10 dilution of a 2
619 mg/mL stock that was spun down to remove protein aggregates) for 6 minutes, then the solution
620 was removed from each well (using a the P1000 pipet and then a P200 for the remanent), washed
621 once with 300 μL of sterile water (water was removed in one strong inversion movement and not
622 pipetted out), then 300 μL of the appropriate cell suspension mixes were gently deposited
623 (consistently on the west side of each well) and allowed to settle gravitationally for 35 min. During
624 cell settlement, fresh 1.5% *w/v* low-melting point agarose (Sigma) was melted in SD-glc in a glass
625 beaker with constant and gentle magnetic stirring. Then, 200 μL of the hot (70°C) agarose solution
626 was taken out (reverse pipetted) with a 1000 μL (blue) tip, held for 10 seconds, and the solution
627 was gently (5 seconds to dispense 200 μL) was deposited in the bottom "west" position,
628 immediately followed by gently pipetting up and down (close to the middle high, also pointing in
629 the west direction). We set a light exposure time of 5 h, which allowed us to observe complete
630 development of the output curves. The total analyzed region was roughly 5.4 mm around the
631 border. Wells have a diameter of 1.554 cm, and cells are embedded in a total volume of 0.5 cm^3 of
632 agarose.

633 **4.6 Flow cytometry**

634 Flow cytometry measurements were performed on an LSR II cytometer (Becton-Dickinson). GFP
635 fluorescence was measured with a 488 nm laser using BD FACS DIVA software (BD Biosciences).
636 First, cells were gated in an FSC-A/SSC- to exclude debris and doublets. GFP-positive cells (either
637 *MAT***a** or *MATα*, depending on the experiment) were gated manually using FlowJo (Becton-
638 Dickinson), and the mean fluorescence of this population was used for further analysis.

639 **4.7 Fluorescence microscopy**

640 Imaging of the half-domain assay was performed using a Leica DMi8 inverted microscope (Leica
641 Microsystems) equipped with a motorized stage and a 20x objective (N.A. 0.4) using *LasX* software
642 (Leica Microsystems) in multi-position mode. Fluorescence images were acquired using the 470/40
643 (Ex), 525/50 (EM) filter for GFP and the TXR filter 560/40 (EX), 630/75 (EM) filter for mApple
644 proteins, respectively. Imaging was also performed using an inverted Olympus IX81
645 epifluorescence microscope equipped with an "Xcite exacte" light source (I = 30%) and a filter cube
646 (EX) 514 nm/10 (EM) 545 nm/40 (49905 – ET) with a 1000 ms exposure time.

647 **4.8 Manual determination of cell-length**

648 As a proxy for the morphological response to pheromone we manually measured the cell-length
649 for cells in the half-domain experiment. In the opto-α experiment, a total of 6995 cells were
650 segmented, while in the oplto-Bar1 experiment the total was 8331 cells (a larger region was sampled
651 in this experiment). In the range plotted the total numbers analyzed correspond to 6686 and 7231
652 cells, respectively. A small fraction of the cells at the leftmost border is taken out to avoid reflective
653 border effects on the accumulation of α-factor (which are not modelled). Lengths were measured

654 manually using the segmented line tool in Fiji in single cells. On each identified cell, we measured
655 its length by drawing a line along its longest diameter. In elongated cells we draw their central
656 longitudinal axis using as many points as needed to maximize precision (elongated cells are
657 curved). Although we counted mostly non-overlapping cells, if a mild overlap existed, or the
658 overlap produced clearly distinguishable boundaries, cells were considered. Prezygotes (cells
659 having a characteristic dumbbell shape, product of cell-cell fusion events), were not considered in
660 the analysis. In samples with large cell-clumps, we measured regions close to empty spaces where
661 little overlap existed. All cell segmentation data and original images are available in Zenodo.

662 **4.9 Machine-learning based cell segmentation.**

663 Manual segmentation is very precise but laborious. We therefore complemented manual
664 segmentation analyses using machine-learning algorithms to obtain additional output data and
665 analyze control half-domain assay experiments. All datasets were pre-processed using rotation,
666 noise insertion, pixel intensity perturbation and translation. Cell segmentation was done on
667 brightfield images on the half-domain assay with two machine-learning algorithms using the U-
668 NET architecture. The first model was used to segment elongated cells and the second model to
669 segment round-shaped cells. The first model was trained on 21 images for 50 epochs. Its accuracy
670 was estimated at 0.97 and its recall at 0.89 (**Fig. S6**). The second model was trained on 10 images for
671 100 epochs and had an estimated accuracy of 0.91 and a recall of 0.73. All the training was
672 performed using a GPU NVIDIA Quadro RTX 4000 (7.5GB RAM memory).

673 After identifying cells as such, round-shaped ones were assigned the category of "receivers" or
674 "emitters" using fluorescence image information. Fluorescently labeled nuclei were also segmented
675 using machine learning. A unique model (same for mApple tagged nuclei and for GFP-tagged

676 nuclei) was trained (with GFP images but as well valid for RFP segmentation) over 30 epochs and
677 its accuracy was estimated to be 0.98.

678 In the opto-α generated gradient (**Fig. 5**), emitters carry a mApple (red) nuclear marker, whereas
679 receivers do not carry a nuclear marker. Cells identified as round with overlapping nuclear
680 segmentation are identified as emitters. In the opto-Bar1-generated gradient (**Fig. 6**), emitters carry
681 a GFP nuclear marker and were identified equivalently. Once all cells were segmented and the
682 receivers (elongated and round shapes) are identified from the emitters, a CSV file that contains
683 information about the identity of the segmented object (receiver or emitter), its position along the
684 experimental axis (in μm), area (in pixels), and the mean GFP intensity in the case of fluorescent
685 reporter receivers is produced (**Fig. 5**). For the latter, background subtraction was performed as
686 follows: a mask was produced that is the sum of the two segmentations from the models for round
687 and elongated shapes. The background then corresponds to the negative part of this mask in the
688 brightfield image. To calculate the orientation of elongated objects, an ellipse was fitted using
689 Python openCV ellipse fitting function and its angle (from 0° excluded to 180°) with respect to the
690 x-axis was extracted (**Fig. 5F, inset**)

691 The data from the nuclei segmentation was used to count haploid and diploids (independently of
692 the shape analysis, which filters cells) as a measure of cell proliferation along the experimental
693 length in the half-domain assay (**Fig. S9**). Counting nuclei allowed us to count individual cells in
694 regions with clumps. It also allowed the easy identification of diploid cells events in the opto-bar1
695 experiment (**Fig. S9**).

696 **5.10 Quantification of the P_{FUS1} transcriptional response in single cells.**

697 Quantification of the P_{FUS1}-GFP response in the half domain assay was more precisely determined
698 segmenting images in the GFP channel, where false positives are minimal. First the images were
699 corrected for illumination inhomogeneities using the BaSiC package for imageJ[57]. The background
700 profile obtained using this tool was equivalent to the background extraction done by ML but
701 performs better in the smaller lengthscale (within-image inhomogeneities). The Cell Profiler
702 software (Broad Institute, Cambridge, MA) was used for the quantification of the transcriptional
703 response. The OTSU adaptive thresholding method was used for object identification in
704 fluorescence images. Cell clumps were discarded with an object-size threshold and a form-factor
705 filter to select rounder objects. Segmentation quality was inspected visually and empirically
706 optimized by changing filter and threshold values. All cell segmentation data and original images
707 are available in Zenodo.

708 **5.11 Data analysis**

709 ***Fitting pheromone gradient generated by the spatial optogenetic induction of α-factor.*** Due to
710 difference in filtering, cell elongation data as well as P_{FUS1} dependent gene-expression at single cell
711 level had to be matched. This was done by binning the data in 100 μm wide bins and taking their
712 mean for the downstream analysis. Fitting was done using the least squares methods on both
713 datasets at the same time, to extract the gradient response parameters λ and C from two $\hat{\theta}(x)$
714 function with different Hill coefficient n, normalization factor A and baseline b. Specifically, n was
715 fixed to 1 for the fluorescence response, and was kept variable and equal to n for elongation. Only
716 integer values between 1 and 7 were considered in the least squares minimization procedure for
717 the n parameter. Fit results are summarized in **Supplementary Table 3** for different values of the
718 Hill coefficient n for cell elongation (and a fixed $n = 1$ for gene expression).

Acknowledgments

The authors would like to thank their team members for their critical reading of this manuscript. This work was mainly supported by the European Research Council grant SmartCells (724813) and received additional support from grants ANR-11-LABX-0038, ANR-10-IDEX-0001-02, ANR-16-CE12-0025-01, and the QLife Institute ANR-17-CONV-0005

Author Contributions

AB conceived the research and contributed to all aspects of this work. MH, CE, SP, CC, and MLB contributed to optogenetic strain construction (MH, CE), experiments (MH, CE, CC), and setup of optogenetic devices (MH, SP, MLB). LC contributed image analysis. VS, YL, WJ and AA contributed the modeling of the pheromone reaction-diffusion dynamics and their fit to experimental data. AB, VS, and PH interpreted the results. AB and PH designed the study. AB, VS, YL and PH wrote the article.

Supplementary Information

Supplementary information contains 9 figures, three tables and the mathematical model.

Bibliography

1. Simsek, M. F. & Özbudak, E. M. Patterning principles of morphogen gradients. *Open Biol.* **12**, 220224 (2022).

2. Stapornwongkul, K. S. & Vincent, J.-P. Generation of extracellular morphogen gradients: the case for diffusion. *Nat. Rev. Genet.* **22**, 393–411 (2021).

738 3. Clark-Cotton, M. R., Jacobs, K. C. & Lew, D. J. Chemotropism and Cell-Cell Fusion in Fungi.
739 *Microbiol. Mol. Biol. Rev.* **86**, e00165-21 (2022).
740 4. Hanson, S. J. & Wolfe, K. H. An Evolutionary Perspective on Yeast Mating-Type Switching.
741 *Genetics* **206**, 9–32 (2017).
742 5. Murphy, H. a & Zeyl, C. W. Yeast sex: surprisingly high rates of outcrossing between asci.
743 *PloS One* **5**, e10461 (2010).
744 6. Wang, X. *et al.* Mating yeast cells use an intrinsic polarity site to assemble a pheromone-
745 gradient tracking machine. *J Cell Biol* **218**, 3730–3752 (2019).
746 7. Wang, X., Pai, C.-Y. & Stone, D. E. Gradient tracking in mating yeast depends on Bud1
747 inactivation and actin-independent vesicle delivery. *J. Cell Biol.* **221**, e202203004 (2022).
748 8. Clark-Cotton, M. R. *et al.* Exploratory polarization facilitates mating partner selection in.
749 *Mol Biol Cell* **32**, 1048–1063 (2021).
750 9. Ghose, D., Jacobs, K., Ramirez, S., Elston, T. & Lew, D. Chemotactic movement of a polarity
751 site enables yeast cells to find their mates. *Proc Natl Acad Sci U A* **118**, (2021).
752 10. Erdman, S. & Snyder, M. A filamentous growth response mediated by the yeast mating
753 pathway. *Genetics* **159**, 919–28 (2001).
754 11. McClure, A. W., Jacobs, K. C., Zyla, T. R. & Lew, D. J. Mating in wild yeast: delayed interest
755 in sex after spore germination. *Mol Biol Cell* **29**, 3119–3127 (2018).
756 12. Reuter, M., Bell, G. & Greig, D. Increased outbreeding in yeast in response to dispersal by
757 an insect vector. *Curr Biol* **17**, R81–R83 (2007).
758 13. Mukherjee, S. & Bassler, B. L. Bacterial quorum sensing in complex and dynamically
759 changing environments. *Nat. Rev. Microbiol.* **17**, 371–382 (2019).

760 14. Banderas, A., Koltai, M., Anders, A. & Sourjik, V. Sensory input attenuation allows
761 predictive sexual response in yeast. *Nat Commun* **7**, 12590 (2016).
762 15. Anders, A., Colin, R., Banderas, A. & Sourjik, V. Asymmetric mating behavior of isogamous
763 budding yeast. *Sci. Adv.* **7**, eabf8404 (2021).
764 16. Bardwell, L. A walk-through of the yeast mating pheromone response pathway. *Peptides* **26**,
765 339–350 (2005).
766 17. Shellhammer, J. P. *et al.* Quantitative analysis of the yeast pheromone pathway. *Yeast* **36**,
767 495–518 (2019).
768 18. Yu, R. C. *et al.* Negative feedback that improves information transmission in yeast
769 signalling. *Nature* **456**, 755–61 (2008).
770 19. Muller, N. *et al.* A Predictive Model for Yeast Cell Polarization in Pheromone Gradients.
771 *PLOS Comput. Biol.* **12**, e1004795 (2016).
772 20. Malleshaiah, M. K., Shahrezaei, V., Swain, P. S. & Michnick, S. W. The scaffold protein Ste5
773 directly controls a switch-like mating decision in yeast. *Nature* **465**, 101–105 (2010).
774 21. Brett, M.-E., DeFlorio, R., Stone, D. E. & Eddington, D. T. A microfluidic device that forms
775 and redirects pheromone gradients to study chemotropism in yeast. *Lab on a Chip* vol. 12 3127
776 (2012).
777 22. Moore, T. I., Chou, C.-S., Nie, Q., Jeon, N. L. & Yi, T.-M. Robust spatial sensing of mating
778 pheromone gradients by yeast cells. *PLoS One* **3**, e3865 (2008).
779 23. Paliwal, S. *et al.* MAPK-mediated bimodal gene expression and adaptive gradient sensing
780 in yeast. *Nature* **446**, 46–51 (2007).
781 24. Segall, J. E. Polarization of yeast cells in spatial gradients of alpha mating factor. *Proc. Natl.*
782 *Acad. Sci. U. S. A.* **90**, 8332–6 (1993).

783 25. Barkai, N., Rose, M. D. & Wingreen, N. S. Protease helps yeast find mating partners. *Nature*
784 **396**, 422–423 (1998).
785 26. Jackson, C. L. & Hartwell, L. H. Courtship in S. cerevisiae: both cell types choose mating
786 partners by responding to the strongest pheromone signal. *Cell* **63**, 1039–1051 (1990).
787 27. Barkai, N., Rose, M. D. & Wingreen, N. S. Protease helps yeast find mating partners. *Nature*
788 **396**, 422–423 (1998).
789 28. Rappaport, N. & Barkai, N. Disentangling signaling gradients generated by equivalent
790 sources. *J. Biol. Phys.* **38**, 267–278 (2012).
791 29. Jin, M. *et al.* Yeast Dynamically Modify Their Environment to Achieve Better Mating
792 Efficiency. *Sci Signal* **4**, ra54–ra54 (2011).
793 30. Diener, C. *et al.* Yeast mating and image-based quantification of spatial pattern formation.
794 *PLoS Comput Biol* **10**, e1003690 (2014).
795 31. Rojas, V. & Larrondo, L. F. Coupling Cell Communication and Optogenetics:
796 Implementation of a Light-Inducible Intercellular System in Yeast. *ACS Synth. Biol.* **12**, 71–82 (2022).
797 32. Motta-Mena, L. B. *et al.* An optogenetic gene expression system with rapid activation and
798 deactivation kinetics. *Nat. Chem. Biol.* **10**, 196–202 (2014).
799 33. Gerhardt, K. P. *et al.* An open-hardware platform for optogenetics and photobiology. *Sci Rep*
800 **6**, 35363 (2016).
801 34. Jacobs, K. C., Gorman, O. & Lew, D. J. Mechanism of commitment to a mating partner in
802 Saccharomyces cerevisiae. *Mol. Biol. Cell* **33**, ar112 (2022).
803 35. Le Bec, M. *et al.* Optogenetic spatial patterning of cooperation in yeast populations. *Nat.*
804 *Commun.* **15**, 75 (2024).

805 36. Doncic, A. & Skotheim, J. M. Feedforward Regulation Ensures Stability and Rapid
806 Reversibility of a Cellular State. *Mol. Cell* **50**, 856–868 (2013).
807 37. Kawada, D. *et al.* The yeast Arf-GAP Glo3p is required for the endocytic recycling of cell
808 surface proteins. *Biochim. Biophys. Acta* **1853**, 144–156 (2015).
809 38. Hilioti, Z. *et al.* Oscillatory phosphorylation of yeast Fus3 MAP kinase controls periodic
810 gene expression and morphogenesis. *Curr Biol* **18**, 1700–1706 (2008).
811 39. Arkowitz, R. a. Chemical gradients and chemotropism in yeast. *CSH Perspect Biol* **1**, a001958
812 (2009).
813 40. Paliwal, S. *et al.* MAPK-mediated bimodal gene expression and adaptive gradient sensing
814 in yeast. *Nature* **446**, 46–51 (2007).
815 41. Moukadiri, I., Jaafar, L. & Zueco, J. Identification of two mannoproteins released from cell
816 walls of a Saccharomyces cerevisiae mnn1 mnn9 double mutant by reducing agents. *J Bacteriol* **181**,
817 4741–4745 (1999).
818 42. Clark-Cotton, M. R. *et al.* Exploratory polarization facilitates mating partner selection in.
819 *Mol Biol Cell* **32**, 1048–1063 (2021).
820 43. Follette, P. J. & Arkowitz, R. A. Chemotropism During Yeast Mating. *Methods Mol. Biol.* **571**,
821 99–110 (2009).
822 44. Ismael, A. & Stone, D. E. Yeast chemotropism: A paradigm shift in chemical gradient
823 sensing. *Cellular Logistics* vol. 7 e1314237 (2017).
824 45. Stone, D. E. & Arkowitz, R. A. In Situ Assays of Chemotropism During Yeast Mating.
825 *Methods in Molecular Biology* 1–12 (2016).
826 46. Arkowitz, R. A. Responding to attraction: chemotaxis and chemotropism in Dictyostelium
827 and yeast. *Trends Cell Biol.* **9**, 20–27 (1999).

828 47. Knop, M. Evolution of the hemiascomycete yeasts: on life styles and the importance of
829 inbreeding. *BioEssays* **28**, 696–708 (2006).
830 48. Boggon, C., Shambat, S. M., Zinkernagel, A. S., Secchi, E. & Isa, L. Single-cell patterning and
831 characterisation of antibiotic persistent bacteria using bio-sCAPA. *Lab. Chip* **23**, 5018–5028 (2023).
832 49. Ni, S., Isa, L. & Wolf, H. Capillary assembly as a tool for the heterogeneous integration of
833 micro- and nanoscale objects. *Soft Matter* **14**, 2978–2995 (2018).
834 50. Benzinger, D. & Khammash, M. Pulsatile inputs achieve tunable attenuation of gene
835 expression variability and graded multi-gene regulation. *Nat. Commun.* **9**, 3521 (2018).
836 51. Jin, M. *et al.* Yeast Dynamically Modify Their Environment to Achieve Better Mating
837 Efficiency. *Sci. Signal.* **4**, ra54–ra54 (2011).
838 52. Liu, Y., Huang, Y., Lu, R., Xin, F. & Liu, G. Synthetic biology applications of the yeast mating
839 signal pathway. *Trends Biotechnol.* **40**, 620–631 (2022).
840 53. Robinson, J. S., Klionsky, D. J., Banta, L. M. & Emr, S. D. Protein sorting in Saccharomyces
841 cerevisiae: isolation of mutants defective in the delivery and processing of multiple vacuolar
842 hydrolases. *Mol Cell Biol* **8**, 4936–4948 (1988).
843 54. Laughery, M. F. *et al.* New vectors for simple and streamlined CRISPR-Cas9 genome editing
844 in Saccharomyces cerevisiae. *Yeast Chichester Engl.* **32**, 711–720 (2015).
845 55. Rivera-Cancel, G., Motta-Mena, L. B. & Gardner, K. H. Identification of Natural and
846 Artificial DNA Substrates for Light-Activated LOV–HTH Transcription Factor EL222. *Biochemistry*
847 **51**, 10024–10034 (2012).
848 56. Zhao, E. M. *et al.* Optogenetic regulation of engineered cellular metabolism for microbial
849 chemical production. *Nature* **555**, 683–687 (2018).

57. Peng, T. *et al.* A BaSiC tool for background and shading correction of optical microscopy images. *Nat. Commun.* **8**, 1–7 (2017).

854 # Figure 1

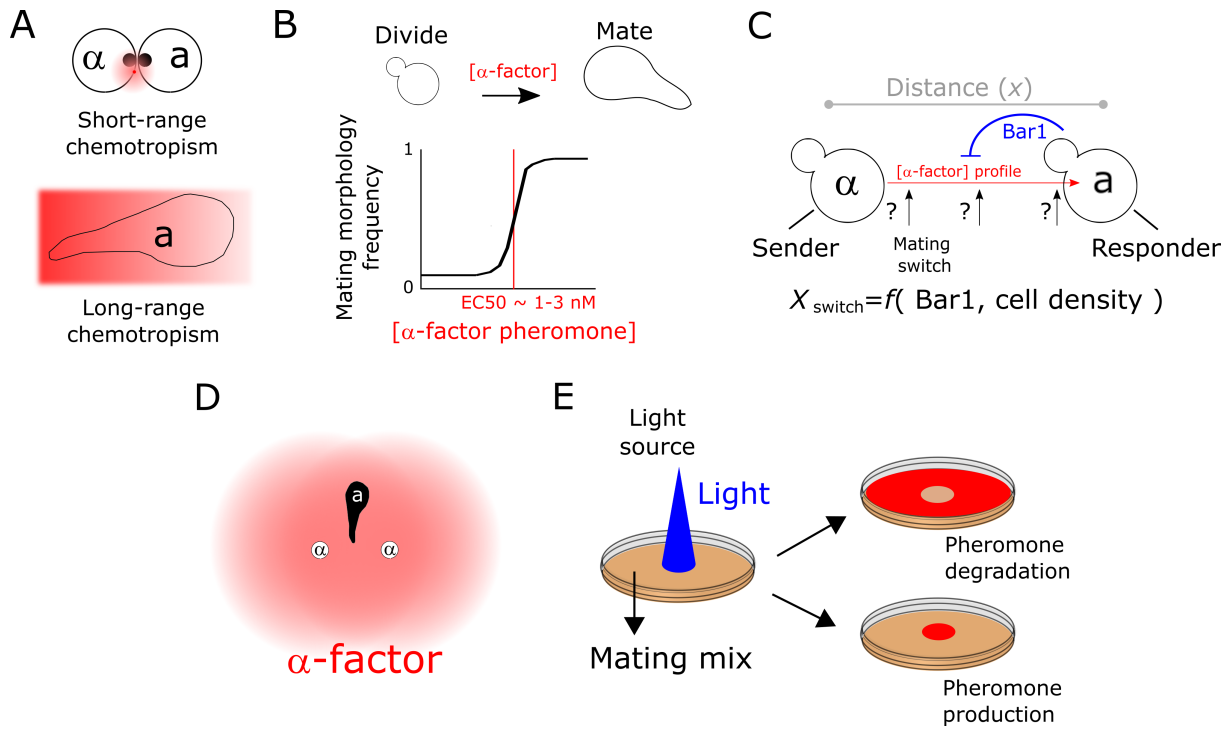

855

856 **Figure 1. Using optogenetics to interrogate the properties of cell-generated signaling gradients.**
857 **A.** Two types of chemotropism have been described in the literature (see text), short range (top)
858 with no cell-elongation involved and frequently observed in mating reactions (black dot represents
859 the polarisome and pheromones—pink halo—are secreted locally), and long-range (displaying cell
860 elongation), seen in artificial pheromone gradients. **B.** The mating switch. Yeast cells switch from
861 budding to mating morphologies when α-factor is present (top). This dose-response is sharp and
862 occurs in the nM range, close to the receptor Kd across strains. **C.** When cells with opposite mating
863 types are located at a distance, the generated α-factor gradient (red arrow, indicating the direction
864 of decay) has a strength (amplitude and steepness) that defines where the concentration is sufficient
865 for switching-on mating behavior. The profile of the α-factor pheromone not only depends on the
866 local density of emitters contributing to the gradient, but also on the presence of the extracellular
867 α-factor peptidase Bar1, and therefore on the density of *MAT***a** cells. When Bar1 is absent or low,
868 the position of the mating switch is expected to happen at a distance. In contrast, if Bar1 is high, the
869 mating switch is displaced towards the source vicinity. **D**. Due to low Bar1 mediated degradation
870 of α-factor when *MAT***a** populations have low density, the α-factor gradients are expected to
871 overlap and provide sufficient intensities to trigger mating behavior at a distance, but at the cost of
872 reduced precision due to "confusing" local maxima. **E.** Optogenetic control of α-factor and Bar1
873 emission allows spatial control of these two opposing activities. In the example shown, a Petri dish
874 containing mating mixes is illuminated in specific regions allowing us to stimulate production or
875 degradation of the pheromone (red color), depending on which genetic determinant is controlled.

Figure 2

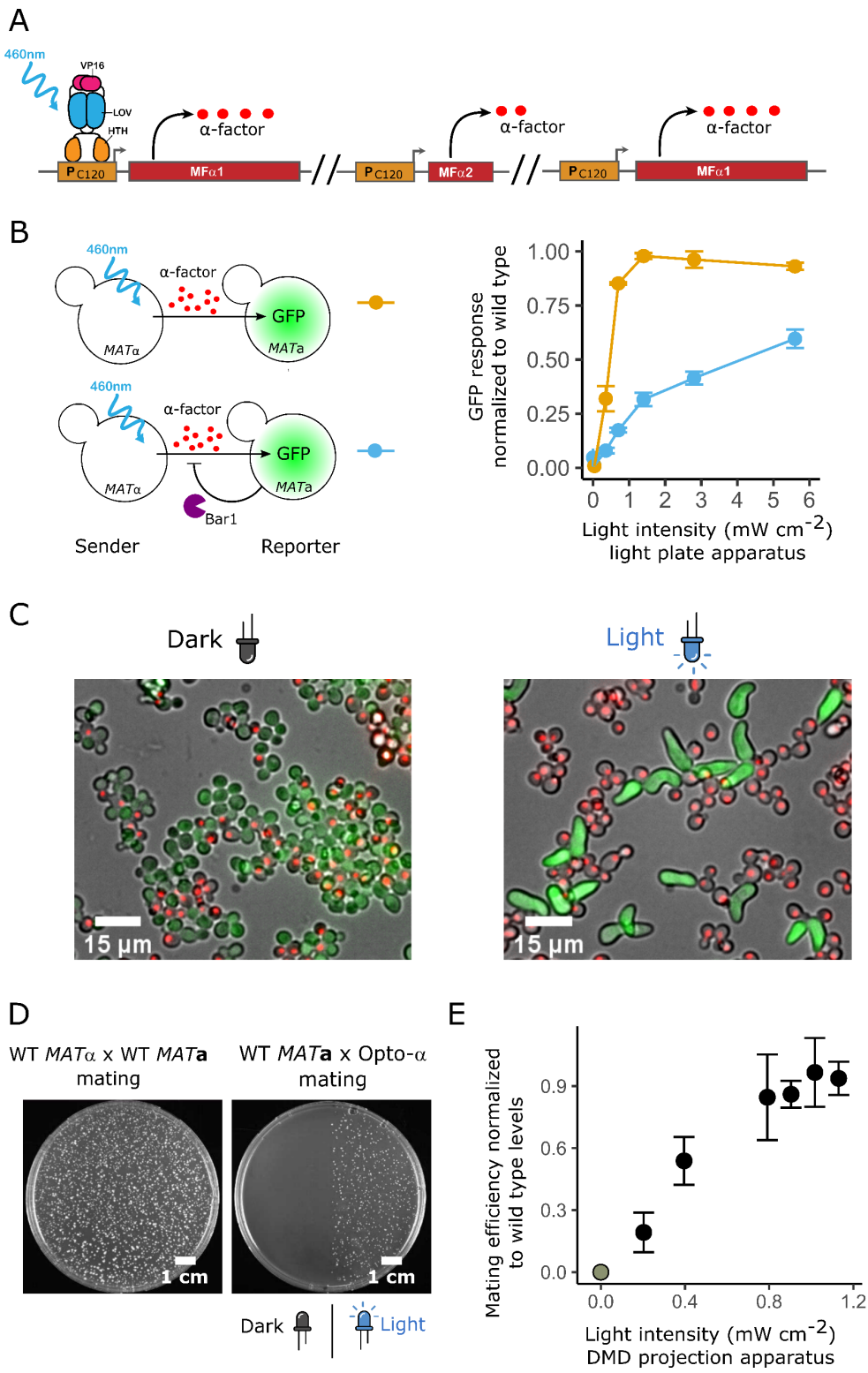
A
460nm
VP16
LOV
HTH
α-factor
α-factor
α-factor
P C120
MFα1
P C120
MFα2
P C120
MFα1
B
460nm
α-factor
GFP
MATα
MATa
460nm
α-factor
GFP
MATα
MATa
Bar1
Sender
Reporter
GFP response normalized to wild type
1.00
0.75
0.50
0.25
0.00
0 1 2 3 4 5 6
Light intensity (mW cm-2)
light plate apparatus
C
Dark
Light
15 µm
15 µm
D
WT MATα x WT MATa mating
WT MATa x Opto-α mating
1 cm
1 cm
Dark
Light
E
Mating efficiency normalized to wild type levels
0.9
0.6
0.3
0.0
0.0 0.4 0.8 1.2
Light intensity (mW cm-2)
DMD projection apparatus

878 **Figure 2. Optogenetic control of extracellular α-factor production allows tight spatial control of**
879 **mating.**

880 **A.** The light-responsive α-factor-producing "opto-α" strain was engineered by replacing the native
881 promoters of the two pheromone-coding genes in *MAT*α (MFα1 and MFα2) with the P_{C120} promoter,
882 which is responsive to the light-activated LOV domain EL222 transcription factor, and by later
883 duplicating the MFα1 (which produces the highest amount of pheromone of the two genes) light-
884 responsive locus. **B.** The activity of the P_{FUS1} pheromone-responsive promoter in *MAT***a** receivers in
885 stirred mating reactions as a function of light intensity. In the assay, the opto-α strain is co-
886 incubated either with *bar1*Δ (top left) or a wild-type *MAT***a** (bottom left) P_{FUS1} GFP reporter strain.
887 After 2 h, the mixes are assessed by flow cytometry. As a control, the reporters are incubated with
888 wild-type *MAT*α, and the baseline-subtracted relative response is calculated (right). Error bars are
889 the SD of n=3 biological replicates. **C.** Agarose-embedded *MAT***a** bar1Δ reporter strains (cells
890 carrying cytoplasmic GFP) co-incubated with opto-α cells (carrying a red nuclear signal expressed
891 by a mApple fluorescent protein) for 5 h under non-illuminated (left) and maximally illuminated
892 (5.8 mW/cm^2, right) conditions. **D, E.** Quantification of mating efficiency through light-controlled
893 pheromone production. Light induces cell-cell fusion in the optogenetic mating assay measured as
894 the appearance of diploid colonies only in illuminated regions (D), which was quantified at
895 different light-doses (E). Efficiency is defined as relative to the activity of the wild-type *MAT*α strain
896 (C). Error bars are the SD of n=3 biological replicates.

Figure 3

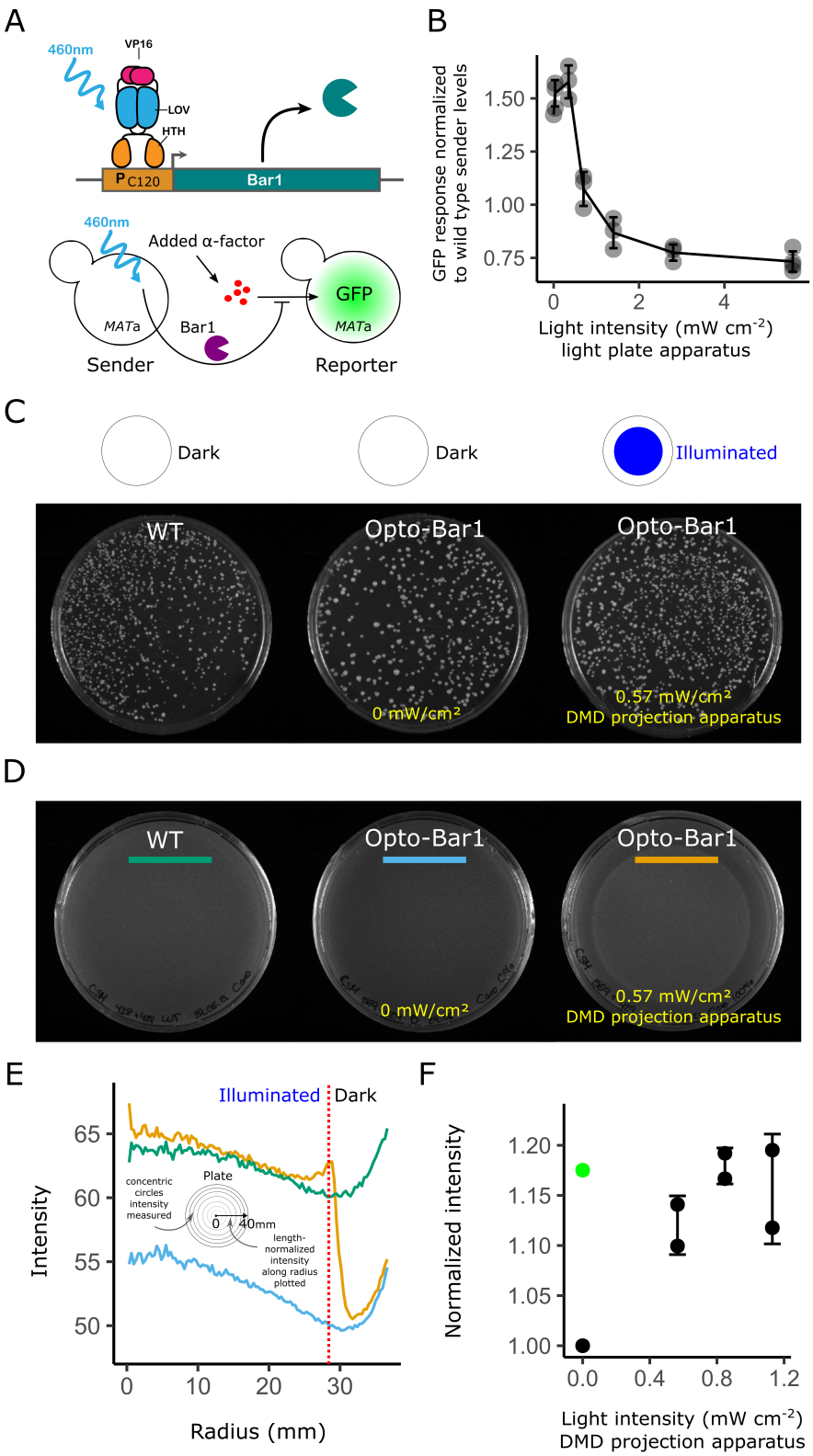
A
460nm
VP16
LOV
HTH
P C120
Bar1
460nm
Added α-factor
GFP
MATa
Bar1
MATa
Sender
Reporter
B
GFP response normalized to wild type sender levels
1.50
1.25
1.00
0.75
0
2
4
Light intensity (mW cm-2) light plate apparatus
C
Dark
Dark
Illuminated
WT
Opto-Bar1
Opto-Bar1
0 mW/cm²
0.57 mW/cm²
DMD projection apparatus
D
WT
Opto-Bar1
Opto-Bar1
0 mW/cm²
0.57 mW/cm²
DMD projection apparatus
E
Illuminated
Dark
Intensity
65
60
55
50
Plate
concentric circles intensity measured
0
40mm
length-normalized intensity along radius plotted
0
10
20
30
Radius (mm)
F
Normalized intensity
1.20
1.15
1.10
1.05
1.00
0.0
0.4
0.8
1.2
Light intensity (mW cm-2) DMD projection apparatus

899 **Figure 3. Optogenetic control of extracellular signal degradation allows tight spatial control of**
900 **growth arrest.**

901 **A.** Promoter replacement in the Opto-Bar1 strain. EL222-mediated light-dependent expression of
902 the native *loci* encoding Bar1 in the *MAT***a** strain (top) and the pheromone activity assay, in which
903 exogenously added pheromone stimulates the sensitized GFP reporter strain (bottom). **B.** Resulting
904 light-dose response from the assay, measured by flow cytometry. The biological activity of the
905 pheromone is defined relative to the activity of the wild-type *MAT***a** strain. Error bars are the SD of
906 3 biological replicas**. C, D.** Diploid selective (C) and non-selective plates (D) showing mating
907 efficiency and growth, respectively in illuminated and dark regions. **E**. Quantification of avoidance
908 of cell cycle arrest ("intensity" corresponds pixel grey value which is proportional to yeast growth)
909 in the Opto-Bar1 strain as a function of the distance from the center (a radius), based on the
910 integrated pixel intensity of a radial profile (traces shown correspond to the colored bars in D, see
911 methods). **F.** Light-dose dependency of cell cycle arrest in Petri-dish assays performed as in D. In
912 this case, growth is normalized to the value of non-activated opto-Bar1 cells (lowest growth).
913 Growth of the wild type is shown as a green dot. Error bars are the SD of two biological replicates.

914

Figure 4

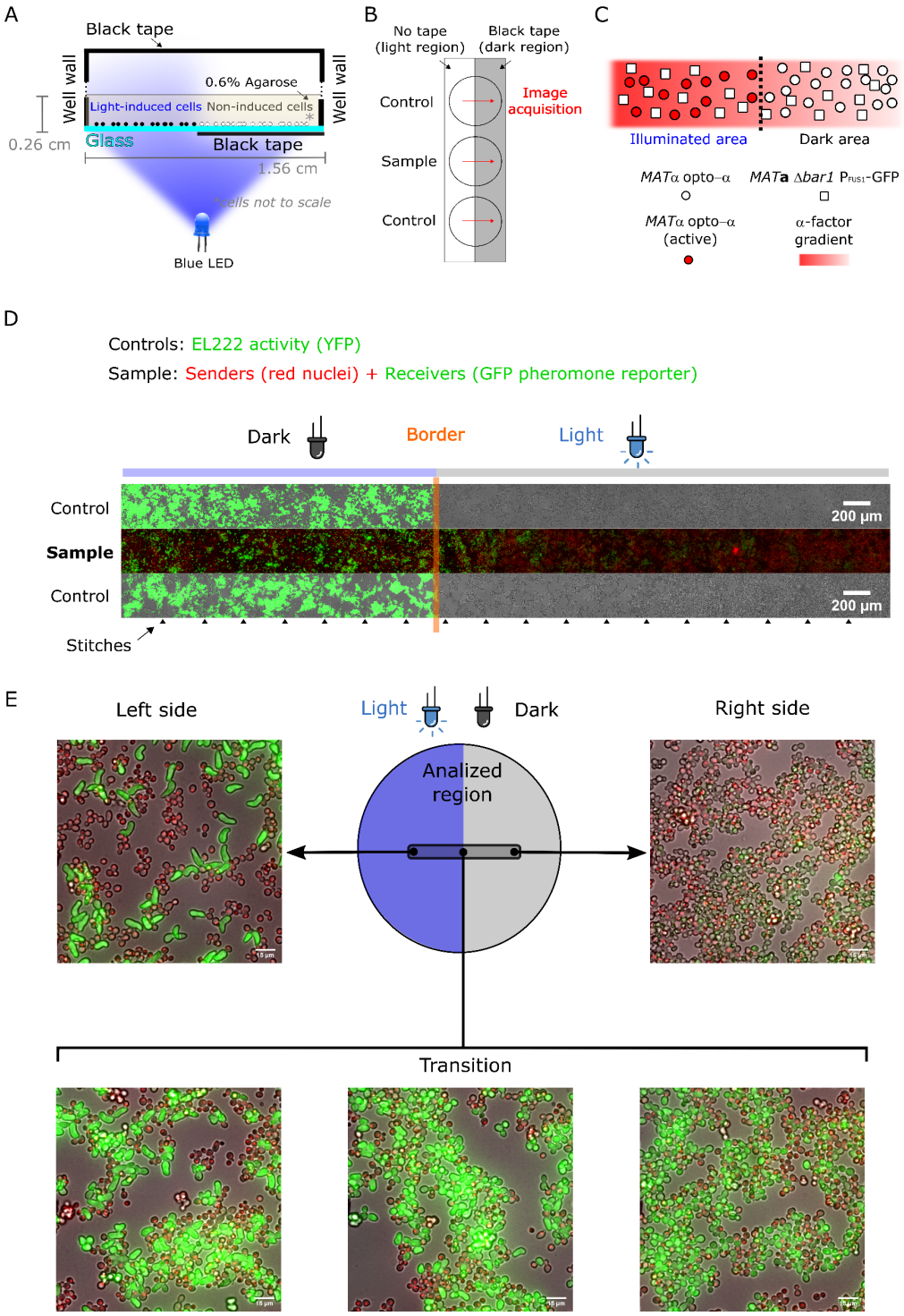

Figure 4. Optogenetic generation of pheromone gradients through the half-domain assay.

A. Half-domain assay. Agarose-embedded cells are located at the bottom of the mini well and half of the glass surface is illuminated to induce EL222-dependent expression. **B.** To determine the position of the light border in samples along the acquisition path (red arrows), a control strain that activates EL222-dependent fluorescent protein expression is run in parallel in adjacent wells. The mean value of the border positions above and below the sample correspond to the position of the light border in the sample. **C.** Schematic representation of the experiment, close to the light-dark transition border. **D.** Microscopy image showing an overview of the mating reaction with the controls for the border location (top and bottom row) displaying strong YFP fluorescence on each side of the mating reaction (center row). Arrowheads at the bottom show where the image was stitched together. In the sample mating reaction (center), opto-α has a red nuclear marker while reporter *MAT***a** *bar1*Δ expresses GFP when stimulated by pheromone. Samples were imaged after 5 h of light exposure. **E.** Example fields along the experimental length showing the increased abundance of elongated phenotypes and the increase in GFP levels in the illuminated region.

Figure 5

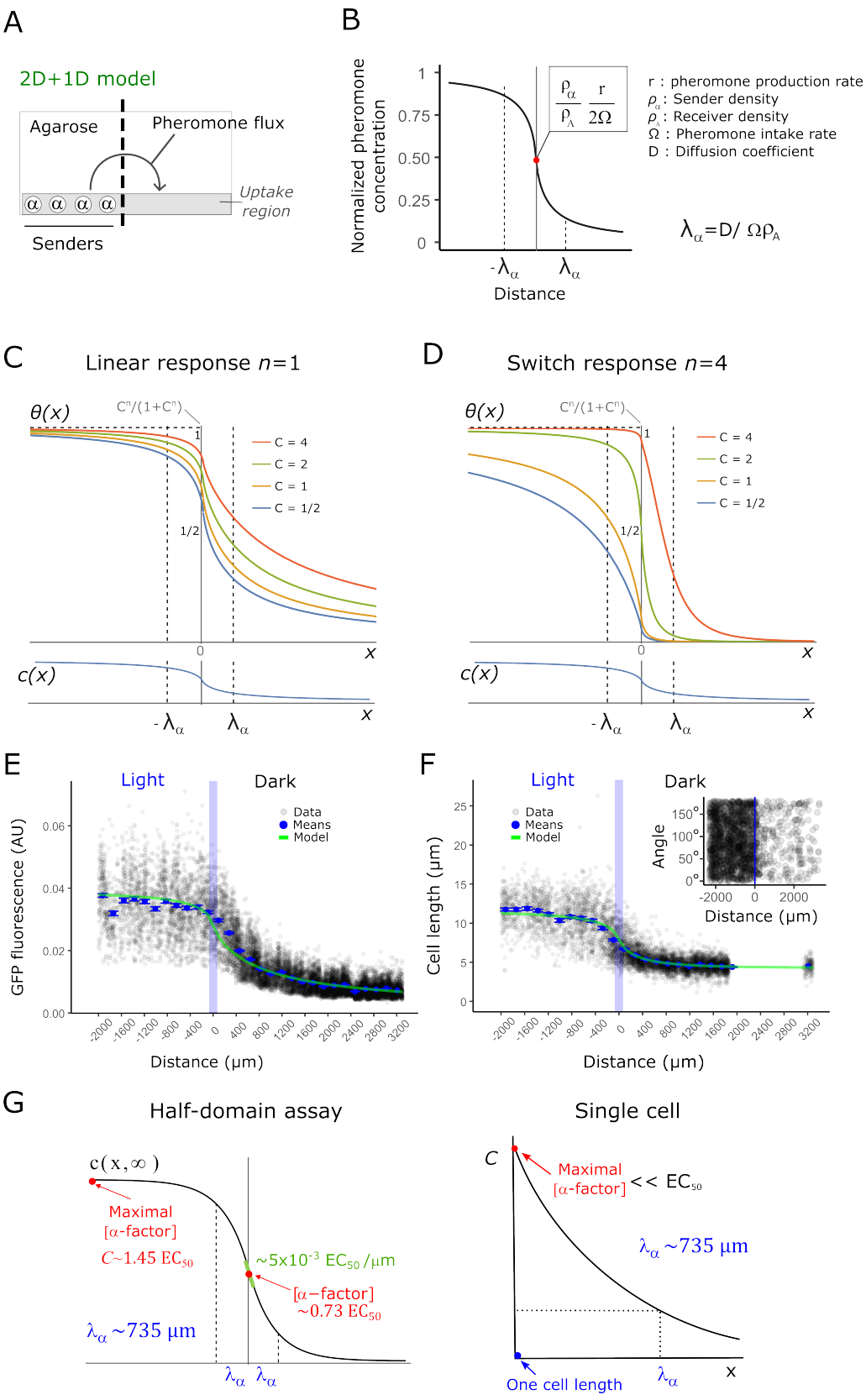
A
2D+1D model
Agarose
Pheromone flux
Uptake region
Senders
B
Normalized pheromone concentration
Distance
r : pheromone production rate
ρα : Sender density
ρA : Receiver density
Ω : Pheromone intake rate
D : Diffusion coefficient
λα=D/ ΩρA
C
Linear response n=1
θ(x)
c(x)
C = 4
C = 2
C = 1
C = 1/2
D
Switch response n=4
E
Light
Dark
Data
Means
Model
GFP fluorescence (AU)
Distance (μm)
F
Cell length (μm)
Angle
G
Half-domain assay
Maximal [α-factor]
C~1.45 EC50
~5x10-3 EC50 /μm
[α−factor] ~0.73 EC50
λα ~735 μm
Single cell
Maximal [α-factor] << EC50
One cell length

933 **Figure 5. Quantitative properties of optogenetically generated gradients recapitulate switch-like**
934 **and linear responses in *MAT*a cells. A.** Schematic representation of the model used to infer α-
935 factor gradient shape. The area on top of the cells is explicitly included and the region where
936 pheromone uptake occurs is restricted to the bottom. **B.** Concentration profile of α-factor at steady
937 state (Eq. 2, See **Supplementary Information**). **C, D.** Normalized response of the receptor (Eq. 3
938 normalized by its theoretical maximal value $C^n/(1+C^n)$) for half-domain expression of α-factor,
939 showing predictions for the shapes of responses using a Hill coefficient equal to n=1 (panel C) and
940 n=4 (panel D). Hill coefficients greater than one correspond to a shift in the response towards a
941 higher concentration of α-factor and a steeper response. **E.** Quantification of single-cell gene
942 expression output (data: black, means: blue) and overlayed model fit (green), with the Hill
943 coefficient set to 1, full set of parameters in Table S3. **F.** Quantification of single-cell gene
944 morphological response (data: black, means: blue) and similarly overlayed model fit (green), with
945 a fitted Hill coefficient of 3, full set of parameters in Table S3. The **inset** shows the absence of
946 gradient alignment of *MAT*a *bar1*Δ. The orientation angle of single cells (points) with large area (a
947 proxy for elongation in the light-domain) respect to the perpendicular to the light-dark transition
948 border. An angle of 0° represents a cell with the long axis of its fitted ellipse oriented perpendicular
949 to the light-dark transition border, while an angle of 90° the same axis is totally parallel. The cutoff
950 for filtering out small cells was 200 pixels. **G.** Population-level and single-cell estimations of
951 pheromone-profile parameters, based on the 2D+1 model.
952

Figure 6

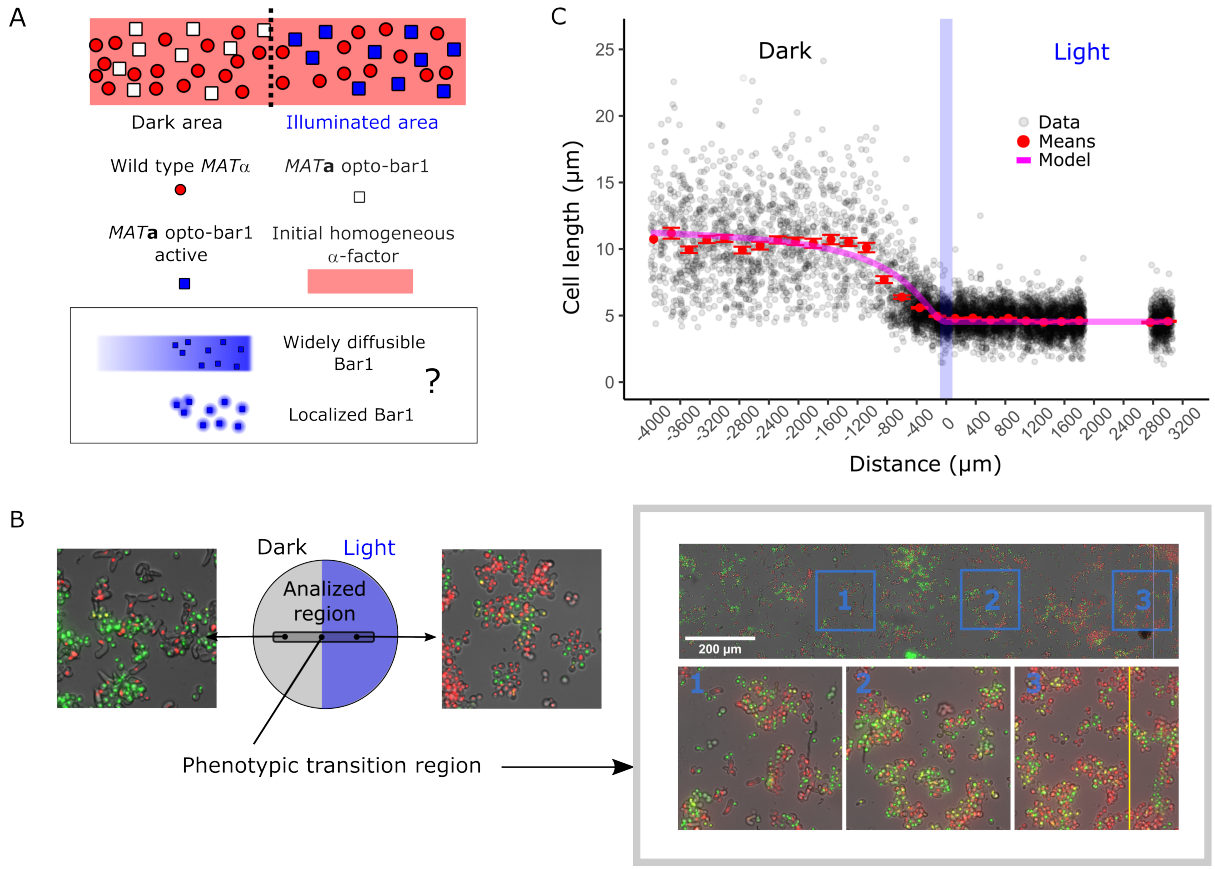

Figure 6. Bar1-generated α-factor gradients reveals restricted Bar1 diffusion. A. Schematic representation of the half-domain assay for opto-Bar1, close to the light-dark transition border. Emitter cells produce α-factor homogeneously. Light-induced Bar1 secretion occurs with unknown spatial distributions (bottom box). **B.** Zoomed-out depiction of the half-domain assay for Bar1 production and microscopy imaging of Bar1 emitters (cells with red nuclei), receivers (cells with green nuclei), and newly formed diploids (cells with yellow nuclei). The yellow line represents the position of the left limit of the light-dark transition border. **C.** Quantification of the single-cell morphological response (cell length) of opto-Bar1. The light border is represented by the blue vertical line corresponding to the border location determined with controls run in parallel (See Methods). The blue dots correspond to the mean value in each one of 30 bins and the error bar represents its standard error. The purple line represents the zero parameter fit of the perfect sink model (see text).